

1 **Geologic Map of Aphrodite Map Area (AMA; I-2476), Venus**

2

3 **V. L. Hansen¹, and I. López²**

4 ¹Department of Earth and Environmental Sciences, University of Minnesota Duluth, 1114 Kirby
5 Drive, Duluth, MN 55812.

6 ² Department of Biology and Geology, Physics and Inorganic Chemistry, Área de Geología,
7 Universidad Rey Juan Carlos. 28933. Mostoles. Madrid, Spain.

8 Corresponding author: Vicki L Hansen (vhansen@d.umn.edu)

9 **Key Points:**

- 10 • We present a geologic map of the Aphrodite map area (0N-57S/60E-180E), representing
11 about 15 percent of Venus' surface
- 12 • The map area records three successive geologic eras: the ancient era, the Artemis
13 superstructure era, and fracture zone complex formation.
- 14 • Deformation and magmatism were the most spatially focused during the youngest era,
15 marked by fracture zone complex formation.
- 16

17 Abstract

18 We present a 1:10M scale geologic map of the Aphrodite Map area (AMA) of Venus (0N-57S
19 /60E-80E). Geologic mapping employed NASA Magellan synthetic aperture radar and altimetry
20 data. The AMA geologic map, with detailed structural elements and geologic units covering over
21 one eighth of Venus' surface, affords an important and unique perspective to test models of
22 global scale geologic processes through time. Geologic relations record a history inconsistent
23 with global catastrophic resurfacing. The AMA displays a regional coherence of preserved
24 geologic patterns that record three sequential geologic eras: the ancient era, the Artemis
25 superstructure era, and the youngest fracture zone era. The ancient era and Artemis
26 superstructure, with a footprint covering more than 25 percent of the surface, are recorded in the
27 Niobe map area to the north. The latter two eras likely overlap in time. The fracture zone
28 domain, part of a globally extensive province, marks the most spatially focused tectonomagmatic
29 domain within the AMA. Impact craters are both cut by, and overprint, fracture zone structures.
30 Twelve percent of AMA impact craters that occur within the fracture zone domain predate or
31 formed during fracture zone development. This observation indicates the relative youth of the
32 fracture zone era and is consistent with the possibility that this domain remains geologically
33 active. The AMA records a rich geologic history of large tract of the surface of Venus and
34 provides an important framework to formulate new working hypotheses of Venus evolution, and
35 contribute to planning future studies of the surface of planets.

36 1 Introduction

37 Nearly 25 years ago, NASA's Magellan mission revealed that Venus lacks plate-tectonic
38 processes [Solomon *et al.* 1992; Solomon, 1993; Phillips & Hansen, 1994], yet Venus' evolution
39 and geodynamic processes remain elusive. Insight into the evolution of Venus and operative
40 geodynamic processes is embedded in the planet surface, laid bare due to Venus' lack of: oceans
41 and hydrosphere and thus extensive erosion and/or associated burial by eroded material; and
42 plate tectonic processes that would result in major portions of the lithosphere (and hence surface)
43 being recycled to the mantle. In addition, Venus' dense atmosphere has protected the surface
44 from globally extensive surface gardening by bolide impact—processes that might result in the
45 formation of thick local to regional regolith.

46 NASA's Magellan SAR data (synthetic aperture radar) provides an unprecedented view
47 of Venus' surface, and provides the primary data for the construction of Venusian geologic
48 maps, which in turn form a fundamental database for a wide range of investigations and future
49 exploration. (We use SAR herein to indicate Magellan SAR).

50 In this contribution we present a geologic map of the Aphrodite Map Area (*I-2476*; 0N-
51 57S/60E-180E). A geologic map of the Niobe Planitia Map sheet (*I-2467*; 0N-57N/60E-180E
52 referred to herein as Niobe Map Area, NMA), adjacent to the AMA but north of the equator will
53 be presented in a separate companion contribution. Geologic mapping of the AMA and NMA
54 were undertaken in a collaborative project. The 1:10M scale of the AMA and NMA is well
55 suited to the large regional scale of Venus geologic domains (Figure 1) [Hansen & López, 2018;
56 Hansen, 2018]. A comparatively similar region on Earth would cover numerous tectonic plate
57 boundaries and include both continental and oceanic crust. The area of the AMA, which covers a
58 120° longitudinal swath across a latitudinal area comparable to a region of the Earth from the
59 equator to ~10° north of the Antarctic Circle, is large enough to capture tectonic domains, yet
60 small enough to provide a relatively detailed view of geologic relations. Geologic maps, unlike
61 raw data sets (e.g., SAR, altimetry and gravity) capture the evolution of a planet's surface.

62 Therefore, geologic maps allow geoscientists to both discover and test models of geologic
63 surface histories and operative geologic processes through time.

64 **2 The Aphrodite Map Area (AMA)**

65 Venus' surface is divided cartographically into 62 1:5M-scale *VMaps* and eight 1:10M-
66 scale *IMaps* (<https://planetarymapping.wr.usgs.gov/Target/project/Venus>). Currently just over
67 half of the *VMaps* have been published. The eight 1:10M map sheets include six sheets each
68 covering 120° longitude on either side of the equator and a N- and S-polar sheet (to N57° and
69 S57°, respectively). This contribution presents the first geologic *IMap* of a Venus.

70 The U.S. Geological Survey published a suite of four 1:10M-scale radar-image mosaics
71 and shaded relief maps of the Aphrodite Planitia region of Venus (*USGS MAP I-2476, 1988*).
72 The four maps are variably referred to as Aphrodite Planitia Region (jacket) and Aphrodite Terra
73 Region (map sheets). Aphrodite Planitia is a misnomer given that no such planitia exists on
74 Venus. In addition, *planitia* refers to a regionally extensive lowland and relatively featureless
75 plain. Aphrodite Terra is also somewhat misleading given that Aphrodite Terra, Venus' most
76 expansive topographically high region, covers a region well beyond the defined cartographic
77 limits of *I-2476* (Figure 1; Mollweide projections). Therefore, we refer to the Aphrodite
78 Planitia/Terra cartographic map area (*I-2476*) herein as the Aphrodite Map Area, or AMA.

79 The AMA encompasses ~60,000,000 km² from 0° N–57° S and 60° E–180° E,
80 encompassing much of *western Aphrodite Terra* south of the equator. Aphrodite Terra,
81 characterized by high topography, straddles the equator and consists of a suite of different
82 geologic features including crustal plateaus western Ovda, Ovda, and Thetis Regiones, volcanic
83 rise Atla Regio, the Diana-Dali corona-chasma chain and Artemis (Figure 1). Artemis Chasma,
84 an ~2000 km-diameter circular trough south of Thetis Regio, lies just east of the center of the
85 AMA and serves as a point of geographic reference for the map area (Figure 2). Topographically
86 the AMA ranges from > 4 to <7 km relative to mean planetary radius (MPR). Crustal plateaus in
87 northern AMA mark the highest elevations, whereas the lowest elevations fall within Diana and
88 Dali Chasmata. A broad trough (~1500-200 km wide, 1-2 km below MPR) concentric to, but
89 outboard of Artemis Chasma and separated from the chasma by a broad concentric high (~1000
90 km wide, up to 1 km above MPR), hosts the regional lowlands within the AMA. The broad
91 trough includes, counterclockwise from the west: Tahmina, Aino, Laimdota, Imapinua, Zhibek,
92 and Nsomeka Planitiae. The Diana-Dali chain cuts the broad topographic trough, with Rusalka
93 Planitia stranded to the north of the other AMA planitiae. North of the equator within the NMA,
94 Llorona, Niobe, Sogolon, and Akhtamar Planitiae might form a northern extension of the broad
95 Artemis-concentric topographic trough (Figs. 1 and 2). Rusalka Planitia marks the northeast
96 corner of the AMA; Manatum Tessera (in western Ovda Regio) anchors the northwest corner.
97 Xaratanga Chasma and Dsonkwa Regio anchor the southwest and southeast corners of the AMA,
98 respectively. The AMA displays a regional zone of chasmata with arms of broadly Artemis-
99 radial chasmata in the southwest to the more regionally focused Diana-Dali chain in the northeast
100 (Figure 2).

101 The AMA contains an assemblage of: (1) ribbon tessera terrain [*Hansen & Willis, 1998*],
102 and other local basal units; (2) suites of radial and concentric structures associated with the
103 formation of the Artemis superplume [*Hansen & Olive, 2010*]; (3) volcanic material including:
104 shield terrain [*Aubele, 1996; Hansen, 2005*], mons/volcano- and corona-related materials,
105 fracture-fed flows, tholi, and undivided flows; (4) regionally extensive 'lineament/fracture zones'
106 that parallel the corona-chasma chains; and (5) 124 impact craters. Ribbon-tessera terrain,

107 Artemis superplume structural suites and fracture zone terrain extend globally beyond the limits
108 of the AMA (Figure 1b).

109 **3 Data and Methods**

110 Global data sets collected during NASA's Magellan mission (1989-1994) provide the
111 basis for modern studies of Venus. *Ford et al.* [1993a] describe Magellan data collection,
112 coverage and interpretation. The Magellan spacecraft, which carried a 12.6-cm wavelength (S-
113 band) radar system to map the surface of Venus, collected three datasets: (1) synthetic aperture
114 radar (SAR) surface images, (2) passive microwave thermal emissivity, and (3) altimetric data.
115 High-resolution Doppler tracking yielded gravity observations. Gravity-topography data provide
116 clues to the nature of long-wavelength (100's of km) subsurface topographic support. Altimetry
117 data (spatial resolution of ~8 km by ~20 km; vertical resolution ~50 m) resolve long-
118 wavelength surface features (10's to 100's of km). SAR data (~100 m/pixel) cover 98% of the
119 surface and provide detailed topographic information suitable for identifying primary and
120 secondary features used for making geologic maps [*Stofan et al.*, 1993; *Hansen & López*, 2018].
121 Magellan data do not provide robust compositional information.

122 3.1 Data employed for geologic mapping

123 The primary data employed in this study, SAR and altimetry data, are available online:
124 <https://atroccloud.wr.usgs.gov/> and https://webgis2.wr.usgs.gov/Venus_Global_GIS/). SAR
125 Cycle 1 (east-directed illumination or left-looking) images cover most of the AMA, with rare
126 local data gaps. Cycle 2 (west-directed illumination, or right-looking) SAR data also covers
127 much of AMA, with three main exceptions from west to east (0N–20S/65–64E; 0N–18S/123–
128 137E; 0N–2S/155–180E). Cycle 3 (left-look stereo) SAR data is quite banded across the AMA,
129 and unavailable south of 43S and from ~93–130E. Digital Compressed Once Mosaicked Image
130 Data Records (C1-MIDR; 225 m/pixel) SAR data from the regional database and map base and
131 digital full-resolution radar map (FMAP; 75–125 m/pixel) data were used in constructing the
132 AMA. Ancillary data include Global Topographic Data Record 3 (GTDR 3) with effective
133 horizontal resolution of 10 km and similar products representing Fresnel reflectivity at 12.6-cm
134 wavelength, average 1- to 10-m-scale slope, and derived 12.6-cm emissivity data (GRDR,
135 GSDR, and GEDR, respectively). GTDR data were combined with SAR images to produce
136 synthetic stereo anaglyphs (*Kirk et al.*, 1992) using NIH-Image macros developed by D.A.
137 Young. These images played a critical role in elucidating the relations between geology and
138 topography and, in particular, the interaction of flows, primary and secondary structures, and
139 topography.

140 Although SAR and altimetry data form the foundation for geologic map construction, we
141 note here a few observations with respect to ancillary slope, reflectivity and emissivity data
142 highlighting broad patterns correlative with various features. Slope data (GSDR) values range
143 from 0 to 15 deg across AMA [*Ford et al.*, 1993a; *Plaut*, 1993] the range in values reflects the
144 wide variation in features. Ridges display linear high RMS slope values, whereas tesserae
145 correlate with a wormy pattern marked by subdued variations in RMS slope values, and coronae
146 typically show circular RMS slope patterns marked by high to intermediate values, with some
147 coronae showing double RMS slope rings. Planitiae exhibit the lowest and most regionally
148 consistent RMS slope values.

149 Reflectivity data (GRDR) display a broad range of values across the AMA. Notable
150 features include ribbon-tessera terrain within Ovda and Thetis Regionae, which are extremely

151 bright in contrast to inliers of ribbon-tessera terrain that correspond to some of the darkest
152 features in the reflectivity data (e.g., Nuahine Tessera and Sudice Tessera). Manatun Tessera
153 (i.e., western Ovda Regio), which sits topographically lower than Ovda and Thetis Regiones
154 (although not in a lowland position), displays reflectivity similar to that of the lowland tessera
155 inliers, although Manatun is quite large relative to the lowland inliers. Chasmata also appear dark
156 in the reflectivity images. Regions of the crustal plateaus with a high density of intratessera flood
157 basin material show intermediate values. Planitiae in southeastern AMA show mostly uniformly
158 intermediate values. Mahuea Tholus (a local high, SE AMA) stands out as an extremely dark
159 feature.

160 Emissivity data (GEDR) shows ribbon-tessera terrain of Ovda and Thetis Regiones as
161 extremely dark, surrounded by regions of intermediate values. Most of the AMA displays
162 intermediate values, with tessera-terrain inliers and chasmata-coronae displaying intermediate-
163 high values. As in the other ancillary data, southeastern AMA displays uniformly intermediate
164 values, with the exception of Mahuea Tholus, which displays intermediate-high values, similar to
165 that of tessera inliers and chasmata.

166 Tessera terrain within the AMA displays different signatures in slope, emissivity, and
167 reflectivity data as a function of regional elevation. Tessera terrain in the high-standing crustal
168 plateaus Ovda and Thetis Regiones have a similar high-value signature in the slope data to the
169 tesserae of western Ovda (e.g., Manatun Tessera) and tessera-terrain inliers (e.g., Nuahine
170 Tessera, Sudice Tessera), however Ovda and Thetis Regiones display low emissivity and
171 extremely high reflectivity compared to (low lying) tesserae that display high emissivity and low
172 reflectivity.

173 3.2 Mapping methodology

174 Geologic maps at all scales should provide the basis for interpreting geologic histories,
175 which in turn provide critical relations for understanding the range of processes that contributed
176 to the evolution of planets [*Gilbert*, 1886]. Construction of a geologic map is a critical first step in
177 unraveling geologic history. Geologic maps are interpretive products used in turn for further
178 interpretation of geological processes [*Compton*, 1985; *Butler & Bell*, 1988; *Maltman*, 1990;
179 *Powell*, 1992]. In the construction of this map we attempt to adhere to historical and contemporary
180 terrestrial mapping methods, with particular attention to complementary criteria, format and
181 cautions outlined for Venus [*Compton*, 1985; *Wilhelms*, 1972, 1990; *Tanaka et al.*, 1994, 2009;
182 *Hansen*, 2000; *Zimbelman*, 2001; *Grindrod & Guest*, 2006]. Throughout mapping we attempt to
183 ensure that map methodology allows that *any* operative process can be *discovered*—that is, the
184 mapping method does not predetermine the resulting geologic map [*Hansen*, 2000]. We
185 distinguish secondary structures (strain) from geologic units given that materials and structures
186 record different ‘time slices’ in the evolution of Venus’ surface, and each reflect different aspects
187 of operative geologic processes [*Wilhelms*, 1972, 1990; *Hansen*, 2000; *Easton et al.*, 2005, 2016].

188 *Hansen & López* [2018] discuss the philosophy and methods of geologic map
189 construction employed herein, including a brief review of Magellan data, SAR image
190 interpretation, and identification and delineation of geologic units and structural elements.
191 Geologic maps constructed using SAR represent high-order derivative products interpreted from
192 clues provided by multiple views (where possible) of the same surface. Given the side-looking
193 nature of SAR, the specific geographic location of mapped features may vary based on employed
194 SAR images; however, the local and regional scale patterns that emerge from mapping using
195 SAR are robust. The methodology for defining geologic units and structural elements/fabrics

196 builds on standard geologic and structural analysis [Wilhelms, 1990; Tanaka, 1994; Hansen,
197 2000; Zimbelman, 2001; Hansen & López, 2018; Peacock & Sanderson, 2018]. Map units
198 represent material interpreted to have been emplaced within an increment of geologic history
199 with limited application of standard stratigraphic methods. However, composite units might lack
200 temporal equivalence across the AMA. In these cases, map units represent descriptive, rather
201 than temporal, units. Thus, designation of a material unit might not imply concurrent or
202 synchronous emplacement. The location and orientation of secondary structural elements are
203 shown independent of material units across the AMA. Evidence for reactivation of secondary
204 structures is common [e.g., DeShon et al., 2000], which further complicates the process of
205 unraveling relative temporal constraints and, ultimately, geohistory.

206 Criteria for distinguishing geologic units include (but is not limited to): (1) the presence
207 of sharp, continuous contacts; (2) truncation of, or interaction with, underlying secondary
208 structures and topography; and (3) primary structures, such as channels or edifice topography
209 that allow a reasonable geologic interpretation and hint at three-dimensional geometry. Some
210 units do not fit these constraints, limiting robust stratigraphic interpretations/implications.

211 Identification and description of map units and structural features result in the generation
212 of a *relative sequence* of material units *independent of absolute time*. This approach is consistent
213 with terrestrial field geology where rock units and geospatial relations are initially identified
214 independent of absolute time. In terrestrial studies, units might be correlated and fit into a historical
215 framework based on universal (*absolute*) time markers (e.g., fossils, radiometric ages,
216 paleomagnetic signatures). Currently there is no means to constrain absolute age on Venus
217 [Campbell, 1999; Hansen, 2000; Hansen & Young, 2007], therefore interpretations of relative
218 temporal relations should stop short of unit correlation, given that correlation requires absolute age
219 constraints. Assessing 'absolute' ages of units and determining the duration of formative processes
220 on planetary bodies (save the Moon) currently relies solely on surface crater density analysis.
221 Given Venus' relatively low global density and large sizes of impact craters robust absolute unit
222 age determination is not possible for Venus [McKinnon et al., 1997; Campbell, 1999].

223 All published 1:5 M-scale USGS Venus geologic maps (Figure 2) were consulted during
224 map construction including: V35/I-2808 [Bleamaster & Hansen, 2005a], V37/I-2752 [Hansen &
225 DeShon, 2002], V46/I-2779 [Stofan & Guest, 2003], and V48/SIM 3099 [Bannister & Hansen,
226 2010]. However, in some cases, map interpretations differ, as happens in the case of geologic
227 mapping on Earth. Discussion of each situation is outside the boundaries of this report.

228 **4 The AMA Geologic Map**

229 This section, which broadly describes the AMA geologic map (Plate 1), is organized
230 from broad to specific. We first present a broad geologic overview, followed by a description of
231 four geologic domains that emerged from map construction. We discuss primary and secondary
232 structures (including tectonic fabrics), and geologic units—including both lithodemic units and
233 material units. We then discuss tectonic suites of structures—that is, structural elements
234 interpreted as displaying genetic relations (e.g., radial or concentric suites). We divide the
235 tectonic suites into local and regional suites, based on suite patterns and geographic distribution.
236 We then briefly describe impact features; impact crater characteristics are presented in Table 1.
237 Map unit descriptions are included on the geologic map, as is a graphical representation of the
238 interpreted sequence of maps units. A brief geologic history of the AMA that emerges from the
239 geologic map completes this report. Feature names referred to herein are shown in figures 1 or 2
240 or on the geologic map. Impact crater names are indicated on the map, with specific location

241 information provided in Table 1. The contribution concludes with first-order observations that
242 emerge from the AMA geologic map.

243 4.1 AMA geologic setting

244 The AMA (Figure 2) encompasses the southern part of western Aphrodite Terra,
245 including western Ovda, Ovda and Thetis Regiones, the Diana-Dali corona-chasmata chain, and
246 Artemis. Southern AMA is dominated by planitiae that collectively define a broad (~150 to 200-
247 km wide) topographic trough concentric to, but outboard of, Artemis Chasma (Figures 1a, 2). A
248 fan of generally ENE-trending chasmata transect the AMA, with the narrow part of the fan (NE
249 AMA) marked by the Diana-Dali corona-chasma chain. The northern chasmata/fracture zone
250 terrain cuts mostly south of Ovda and Thetis Regiones and north of Artemis (Ralk-umigu and
251 Quilla Chasmata); whereas the fan of chasmata radial to Artemis spays along three zones:
252 Gamsilg and Juno chasmata, Xaratanga Chasma, and Reita Chasma, counterclockwise from
253 ~8:30 to 6:30. Chasmata are more widely spaced and distributed, and less well-defined
254 topographically in the southwest, as compared to Diana-Dali Chasmata. Southeastern AMA, a
255 relatively featureless region, hosts Dsonkwa Regio marked by subdued topography (challenging
256 its ‘regio’ moniker), and Mahuea Tholus notable in its isolation, steep local slopes and well-
257 defined flow features [Moore *et al.*, 1992].

258 4.2 Geologic domains

259 The AMA is divisible into four major geologic domains (1-4) that locally overlap: (1)
260 crustal plateaus (western Ovda, Ovda, and Thetis Regiones) and lowland inliers of ribbon tessera
261 terrain [Hansen & Willis, 1998; Hansen & López, 2010]; (2) Artemis, including Artemis Chasma
262 and the interior region, and a huge radial dike swarm and a concentric wrinkle ridge suite, 12,000-
263 and 13,000-km diameter, respectively [Hansen & Olive, 2010]; (3) ‘fracture zones’—broad zones
264 (100’s of km wide and thousands of km long) of deformation marked by a combination of fractures
265 (broadly defined), coronae, and chasmata; and (4) southeastern AMA, which is cut by Artemis-
266 radial fractures, and hosts both shield terrain [Aubele, 1996; Hansen, 2005] and extensive tracts of
267 thin flows cut by Artemis-concentric wrinkle ridges.

268 4.2.1 Domain 1

269 Ribbon tessera terrain [Hansen & Willis, 1998], and other basal regions mark some of the
270 oldest recognizable crustal exposures across the AMA. These are best preserved in elevated crustal
271 plateaus, although exposures occur across much of the AMA preserving an early record of crustal
272 evolution [Hansen & López, 2010]; southeastern AMA generally lacks ribbon-tessera terrain,
273 although other basal units occur locally. These basal units could be temporally correlative to
274 ribbon-tessera formation; relative time is unconstrained.

275 4.2.2 Domain 2

276 Domain 2, marked by two suites of Artemis-centric structures—radial fractures and
277 concentric wrinkle ridges, as recognized by Hansen & Olive [2010], occurs across essentially the
278 entire AMA and NMA. These two suites of structures, and their relations with regional units are
279 best preserved in southeastern AMA, an area relatively unaffected by younger events. In some
280 locations Artemis-radial fractures are well developed; elsewhere, Artemis-concentric wrinkle
281 ridges dominate. Regardless, it is clear that these two suites of concentric and radial structures are

282 genetically related to one another [*Hansen & Olive, 2010*] Detailed and regional cross-cutting
283 relations indicate that fractures began to form before wrinkle ridges, and that the fractures likely
284 served as conduits for Artemis-fed flows (unit Afu) distributing flows locally across huge regional
285 areas. Areas buried by these flows, as well as regions covered by a thin cover of shield terrain
286 [*Aubele, 1996; Hansen, 2005*], were later deformed by the suite of Artemis-concentric wrinkle
287 ridges. Locally Artemis-radial fractures are buried, and in some cases these fractures were
288 reactivated as inversion structures [e.g., *DeShon et al., 2000*]. Artemis-radial fractures locally
289 occur as buried lineaments. Artemis-fed flows lack indications of flow morphology, perhaps due
290 to simple leaking to the surface as a result of the magmatic head intersecting the local surface
291 [*Head & Wilson, 1991*]. These flows were likely characterized by low viscosity, based on the
292 general lack of flow features. Alternatively, flow feature definition was lost through time [e.g.,
293 *Ardivson et al., 1992*].

294 A broad topographic trough (~6,500-km diameter), concentric to Artemis Chasma, hosts
295 wrinkle ridges within the trough low. Radial fractures are locally preserved in a concentric region
296 on either side of the trough. Collectively relations indicate that the trough and outer topographic
297 high probably formed during Artemis superstructure evolution with Artemis-fed ‘flows’ occurring,
298 or collecting, more in the broad trough.

299 4.2.3 Domain 3

300 This domain cuts diagonally across the AMA from the southwest to the northeast, where it
301 intersects with fracture zones that radiate from the volcanic rise Atla Regio. Fracture zones,
302 including those in the AMA, recognized in early studies of Magellan global data are referred to as
303 rifts, or rift zones in some published literature [e.g., *Price & Suppe, 1994, 1995*]. However, detailed
304 mapping within portions these zones indicates that the zones do not record large extensional strain
305 perpendicular to regional fracture trends, as is the case of terrestrial rift zones [*Hansen & Phillips,*
306 *1993; Hansen & DeShon, 2002*]. Furthermore, these zones are typically much wider (i.e., normal
307 to trend) than terrestrial rift zones (locally >1000 km wide), and the nature of the linear structures
308 (in map view) within the zones differ from normal faults developed in typical terrestrial rift zones.
309 Therefore, we refer to these regions as ‘fracture zones’, following terminology of *Hansen &*
310 *DeShon* [2002]. The fracture zone domain is characterized by penetratively deformed zones
311 marked by lineaments consisting of fractures, graben, pit chains, stoped troughs, hybrid structures
312 (*see description below*), and coronae and chasmata. The fracture zones and associated structures
313 dominantly post-date the formation of the Artemis-centric fractures and wrinkle ridges (e.g.
314 domain 2). AMA hosts three types of coronae, with hybrids between three end members: (A)
315 coronae marked by concentric structures; (B) radial fracture coronae; and (C) coronae with obvious
316 corona-sourced flows. Radial and concentric fractures represent fractures/graben/dikes and/or
317 magmatic stoping structures; in general, magma locally remained at depth, but emerged to the
318 surface in the case of coronae with surface flows. Coronae type may be related to local lithospheric
319 thickness, and the ability to support volcanic edifices and surface flows [*McGovern et al., 2015*].

320 The fracture/corona/chasma zones define regions of variable deformation along linear to
321 fan-shaped areas with the shape and orientation of each fracture zone broadly paralleling the trend
322 of its internal structural lineament fabric. The most prominent zone, the Diana-Dali corona-chasma
323 chain, trends ENE in the east extending northeast to volcanic rise Atla Regio (outside AMA; Figs.
324 1 and 2); west of Miralaidji Corona this zone splays into two zones. The southern arm trends WSW
325 to SSW marked by the alignment of Bona, Mayael, Colijnsplaat, Annapurna, and Teteoinnan
326 Coronae. The northern arm extends west through Ceres Corona. West of Ceres the zone splays

327 again, with one arm trending NW to Blai Corona. A more prominent arm, which we refer to
328 informally as the Vir-ava/Ralk-umgu chasma zone, extends westward from Ceres Corona, trending
329 WSW to W and curving to the WNW northwest of Artemis. The Vir-ava/Ralk-umgu chasma zone,
330 which displays extensive development of extremely closely-spaced lineaments, includes Quilla,
331 Vir-ava, Jana, Ralk-umgu, and Kuanja Chasmata. Inari Corona lies along this trend between Vin-
332 ava Chasma to the north and Quilla Chasma to the south. Much of the zone cuts south of Thetis
333 and Ovda Regiones, but NW-trending portions dissect ribbon-tessera terrain both within Ovda
334 Regio, and the region between Thetis and Ovda Regiones. Directly north and west of Artemis the
335 Vir-ava/Ralk-umgu chasma zone is characterized by extreme penetrative development of linear
336 troughs and pit chains, which collectively likely represent magmatic stoping [Hansen & López,
337 2014a, 2014b]. The Vir-ava/Ralk-umgu chasma zone is similar in character to the Diana-Dali
338 corona-chasma chain, although it is generally lacking in the development of coronae (with the
339 exception of Inari Corona). The fracture zones take on a different character where the zones dissect
340 ribbon-tessera terrain and crustal plateaus. The lineaments, which are more widely spaced as
341 compared to other portions of the fracture zone, become more difficult to delineate, due in part to
342 the tessera-terrain host, and its characteristic ribbon-tessera terrain fabric. A possible north-
343 trending zone anchored by Rosmerta Corona in the south, may also form part of a fracture zone,
344 although this zone lies mostly in the NMA, and is characterized by coronae rather than fractures
345 or other lineaments [López & Hansen, 2015; Hansen & López, 2018].

346 West of Artemis Chasma, fracture zones take on a more fan-like character. One spoke,
347 marked by penetratively-developed lineaments, trends SW (7 o'clock relative to Artemis Chasma)
348 includes Reitia Chasma and Triglava Corona. A second spoke that trends west from Artemis
349 Chasma (9 o'clock) is marked by Juno Chasma, Gefjun and Tai Shan Coronae, and Kunapipi
350 Mons. Southwestern AMA hosts numerous coronae that are broadly aligned along these fracture
351 zones; coronae structures and flows locally mask extensive parts of the fracture zones.

352 The Diana-Dali arm, which sits along a ~3000 km-wide linear topographic high that trends
353 toward Atla Regio, is characterized by extremely penetrative deformation across an ~2000-km
354 wide band. This zone hosts AMA's largest coronae; associated chasmata form deep troughs
355 marked by steep scarps. These coronae display radial and concentric fractures, with variable
356 development of flows. The easternmost coronae display more flows; whereas fractured surfaces
357 and a notable lack of flows, characterize the coronae closer to Artemis. Coronae developed along
358 the fracture zone periphery display more prominent flows, perhaps due more to the relatively lower
359 intensity of deformation than to the nature of the flows. The relatively high elevation across the
360 Diana-Dali belt is consistent with the occurrence of relatively thin lithosphere [Rosenblatt *et al.*,
361 1994], which is in turn consistent with the formation of coronae characterized by subsurface
362 magmatism, as opposed to surface flows [McGovern *et al.*, 2015]. The relative size of the coronae
363 is likely due to the broad width of thin lithosphere (i.e., high elevation)—that is, thin lithosphere
364 across an expansive region allows for the development of large coronae given that the relatively
365 thin lithosphere favors development of coronae over large volcanic constructs [McGovern *et al.*,
366 2015].

367 The broad fan-shape region west of Artemis Chasma hosts both coronae and fracture zones;
368 overall deformation here is more distributed, or less penetratively developed than in the other
369 fracture zones. This region is also topographically subdued, consistent with thicker lithosphere
370 [Rosenblatt *et al.*, 1994]. Coronae in this part of AMA variably display radial and concentric
371 structures and surface flows. Corona-radial fractures and corona-concentric fractures are best
372 developed along trends parallel to the local orientation of Artemis-radial fractures, or the spokes

373 of the fracture zones; in contrast, corona-concentric fold suites are best developed parallel to the
374 local orientation of Artemis-concentric wrinkle ridges (that is, perpendicular to the trend of the
375 aforementioned fracture suites). Most coronae within this region display corona-sourced flows,
376 and observation consistent with a thicker lithosphere across this region [McGovern *et al.*, 2015],
377 compared to that of the Diana-Dali corona-chasma chain, or to the mostly corona-free, Vir-
378 ava/Ralk-umgu chasma zone.

379 The Vir-ava/Ralk-umgu chasma zone, ~1,000 kilometers wide and up to 3,000-4,000
380 kilometers long, includes a single corona, Inari. This fracture zone is characterized by extremely
381 penetratively developed (that is, closely-spaced) pit chains, linear troughs, fractures, and hybrid
382 features (described in tectonic structures section). The lineaments are so penetratively developed
383 that host material cannot be defined. However, despite the incredible high lineament density, flows
384 that locally bury earlier-formed lineaments are notably rare [Hansen & López, 2014a, 2014b;
385 Tovar *et al.*, 2015].

386 4.2.4 Domain 4

387 Southeastern AMA differs from the other domains in that it is defined by area, and a
388 general lack of features. Southeastern AMA is free of crustal plateaus and hosts limited basal
389 terrain, and lacks both true coronae and fracture zones. This area preserves an excellent record of
390 the spatial and temporal development of Artemis-radial fractures and Artemis-concentric wrinkle
391 ridges. The limited exposures of basal terrains offer windows in time—providing local,
392 fragmented records of surface evolution prior to the formation of the Artemis superplume.
393 Within domain 4, Artemis-radial fractures display incredible continuity, extending for 2000-3000
394 km; the structures are locally buried, yet reappear along trend, either as exposed fractures, or as
395 veiled, shallowly buried lineaments. Where Artemis-radial fractures are best developed, wrinkle
396 ridges do not form; and where wrinkle ridges are best developed, fractures are clearly buried.
397 Dsonkwa Regio (probably not a true regio as noted previously) hosts Tonatzin and Utset
398 ‘Coronae’ and limited exposures of ribbon-tessera terrain (including Shait Tessera) and other
399 basal terrains, which may represent shallowly-buried ribbon tessera. Tonatzin Corona lacks
400 radial fractures and concentric structures, defined instead mostly by a shield field; it is not clear
401 why Tonatzin is considered a corona, and this classification should be revisited. However, we
402 preserve the name of Tonatzin Corona herein given that detailed mapping of this feature is
403 outside the scope of the current project. Utset Corona is marked by concentric structures, and
404 two suites of fractures, one parallel to local Artemis-radial fractures and another suite near
405 orthogonal to this trend (NNE). Classification of Utset as a corona might also be suspect.
406 Dsonkwa Regio marks a local exposure of regional basal terrain cut by Artemis-radial fractures
407 and surrounded by lower regions covered by thin flows deformed by Artemis-concentric wrinkle
408 ridges. Domain 4 provides an excellent example of the type of terrain/unit contacts across the
409 AMA, as discussed in the section Terrain Units. Mahuea Tholus is perhaps the most prominent
410 feature in domain 4. Urd Tessera, which lies nearly due east of Mahuea Tholus, marks a basal
411 terrain, a small local high surrounded by younger flows cut by Artemis-concentric wrinkle
412 ridges. Contrary to its name Urd Tessera does not host ribbon-tessera terrain, but rather is
413 characterized by closely-spaced NNW-trending folds and NNE-trending lineaments. The NNE-
414 trending lineaments are not ribbon structures however, nor are these structures orthogonal to the
415 fold trends, as would be expected in the case of typical ribbon tessera terrain [e.g., Hansen &
416 Willis, 1998].

417 4.3 Primary structures, secondary structures, and tectonic fabrics

418 Structures, both primary (depositional or emplacement-related) and secondary (tectonic),
419 are identified in SAR data. Tectonic fabrics represent suites of genetically related secondary
420 structures that together define a coherent structural pattern.

421 4.3.1 Primary structures

422 Primary structures on Venus are mostly related to volcanic features and include channels,
423 shields, pits and pit chains, lobate flow fronts and flow levees, and impact crater haloes and rims
424 [Ford *et al.*, 1993b]. However, some of these features may result from sediment
425 deposition/erosion processes. More detailed work will be required to clarify the formation of all
426 these features.

427 Channels (or canali) are sinuous, low-backscatter troughs tens to hundreds of kilometers
428 long and a few kilometers wide; locally, they may lack apparent topographic relief, and are
429 interpreted to form by channelized fluid flow [Baker *et al.*, 1992, 1997; Komatsu & Baker,
430 1994]. The nature of the fluid is undefined, as is the type of erosion, whether mechanical or
431 thermal, cutting downward from the surface, or upward from depth [e.g., Gregg & Greeley,
432 1993; Bussey *et al.*, 1995; Williams-Jones *et al.*, 1998; Jones & Pickering, 2003; Lang &
433 Hansen, 2006]. Channels could be primary structures, related to levee development during flow
434 emplacement, or channels could be erosional structures in which case they would post-date the
435 emplacement of the units they cut. The formation of these features is not understood [Baker *et al.*
436 *et al.*, 2015]. Multiple mechanisms could contribute to channel formation—that is, channels across
437 the AMA might not share a singular origin [Hansen & López, 2018].

438 Shields are small (generally 1 to 15 km in diameter, rarely 20 km in diameter), quasi-
439 circular to circular, radar-dark or radar-bright features with or without topographic expression
440 and with or without a central pit, interpreted as small volcanic edifices [Guest *et al.*, 1992;
441 Crumpler *et al.*, 1997; Addington, 2001]. The size of individual shields is difficult to constrain
442 because the bases of individual shields are typically poorly defined, and deposits commonly
443 blend smoothly into a composite layer [Hansen, 2005].

444 Lobate flow fronts and flow levees can indicate local surface flow direction providing
445 information about flow emplacement and local paleo-topography at the time of flow
446 emplacement, unless deposits represent pyroclastic flows. Flow directions, interpreted from
447 lobate flow fronts and levees, are shown on the map.

448 Impact craters are perhaps most prominently marked by rims that sit above circular
449 interiors and within/at the boundary of ejecta material that occurs as extremely radar-bright
450 deposits [Weitz, 1993]. Impact craters can also display haloes, radar-bright (rough) or radar-dark
451 (smooth) deposits that extend outward from the rim and ejecta deposits up to many crater diameters
452 [Izenberg *et al.*, 1994]. Haloes are thought to form as a result of the shock-induced crushing of
453 host material just preceding or accompanying bolide impact or due to accumulation of fine-scale
454 ejecta. Some craters have parabolic haloes, which can extend up to 20 crater radii to the west; these
455 thin deposits(?) are interpreted as due to the interaction of east-to-west zonal winds [Arvidson *et al.*
456 *et al.*, 1991, 1992; Campbell & Campbell, 1992]. The nature and extent of impact haloes might be
457 leveraged to provide unique clues about regional geologic histories [Campbell *et al.*, 2015; Whitten
458 & Campbell, 2016].

459 Crater haloes and parabolic deposits appear to degrade with time losing their radar contrast
460 with surrounding terrain [Izenberg *et al.*, 1994]. Impact craters that display both extreme haloes
461 and radar bright crater interiors are generally interpreted as relatively young, whereas craters with

462 degraded haloes, or lacking haloes entirely, and displaying radar smooth filled interiors are
463 interpreted as relatively old [Phillips & Izenberg, 1995; Herrick & Rumpf, 2013]. Impact crater
464 haloes are indicated on the map with a stippled map pattern so that underlying units and structures
465 can be represented along with the extent of crater haloes.

466 4.3.2 Secondary structures

467 Secondary structures form after the emplacement of geologic units and typically record
468 tectonic processes; accordingly, these structures provide clues for formational tectonic processes.
469 The distribution and (or) character of secondary structures may also provide clues for the
470 delineation of material units, as well as temporal relations between different material units
471 [Hansen, 2000; Tanaka et al., 2009; Hansen & López, 2018]. Most radar lineaments represent
472 secondary structures. Stofan et al. [1993] provided an excellent introduction to the interpretation
473 of secondary structures in SAR imagery. Secondary structures within AMA include various types
474 of lineaments, fractures and faults; pits and pit chains, stoping troughs, and hybrid structures; folds,
475 ridges, chasmata, and wrinkle ridges. Given that the AMA covers ~60,000,000 km² we do not
476 show all lineaments. However, we attempt to capture the essence of recognized structural suites.
477 Therefore, in some cases lineament trends will be shown, in other cases each lineament is shown,
478 in yet other cases a collection of the lineaments is shown on the map. There is no single unique
479 scale of lineament or feature identification, just as there is not a single unique scale of observation
480 in the case of field-based mapping on Earth, particularly for maps that cover huge areas of Earth's
481 surface.

482 Fractures are sharply defined lineaments with a negative, or null, topographic signature,
483 commonly grouped into suites based on orientation, pattern (i.e., radial or concentric) and/or
484 spacing (i.e., widely spaced or closely spaced). Fractures are generally interpreted as extensional
485 structures [Banerdt et al., 1997] although there might be very little measurable extension normal
486 to their trends. Locally fractures consist of *en echelon* fractures indicative of either a shear
487 fracture origin, or the emergence of a fracture at depth to the surface with the *en echelon*
488 fractures marking hackles. Any consideration of fractures as evidence of tectonic extension
489 should be independently and robustly proven; we do not consider fractures to be extensional
490 structures in the same mode as, for example, normal faults, herein.

491 Pits—sharply defined depressions, occur individually, or more commonly as pit chains—
492 linear arrays of pits. Pit chains can have a distinctive scalloped plan-view, or be marked by
493 straight, sharply defined parallel walls forming a generally flat-floored trough, given complete
494 connection or coalescing of a chain of pits. Pits or pit chains can be considered primary
495 structures or secondary structures, depending on the question at hand. Pit chains are primary
496 structures relative to pit-related materials, yet they may be secondary structures relative to the
497 units they cut or are emplaced within. Pit chains, which represent regions marked by subsurface
498 excavation, may mark the surface expression of dilatational faults or dikes [Grosfils & Head,
499 1994; Okubo & Martel, 1998; Bleamaster & Hansen, 2005b; Ferrill et al., 2004; Schultz et al.,
500 2004] or they could represent stoping features that would not require associated crustal extension
501 [e.g., Cushing et al., 2014]. Pit chains, or stoping troughs may evolve from fractures, dikes, or
502 faults; these features may or may not result in crustal extension. Pit chains may evolve into
503 shallow troughs, marked by paired, closely spaced (<5 km and commonly ≤ 1 km) lineaments
504 marking a shallow (tens of meters) flat depression bounded by steep sides; they are interpreted
505 herein as the result of subsurface magmatic activity [e.g., Bannister & Hansen, 2010; Hansen &

506 *López, 2018*]. A full discussion of pit chains and trough structures is outside the goals of this
507 contribution.

508 Folds are ridges defining wave-like topographic expression marked by a gradational radar
509 character normal to their trend [*Stofan et al., 1993*]. Folds are generally interpreted as
510 contractional structures, although folds locally form in extensional environments in terrestrial
511 settings. Small ridges are topographic ridges with low relief and width, similar in appearance to
512 folds except that the nature of the lineament is ambiguous—although possibly of contractional
513 origin (marked by folds or thrust faults). Large ridges are topographic ridges with moderate relief
514 and width. Ridges and chasmata (relatively wide topographic troughs) commonly occur as paired
515 structures within AMA, particularly within the corona/chasmata chains and fracture zone
516 domain. Scarps are marked by a steep slope.

517 Wrinkle ridges define low sinuous spines spaced a few kilometers to tens of kilometers
518 apart and up to a few hundred kilometers long; these lineaments, which represent low (<2%)
519 layer contractional strain, are found on most terrestrial worlds, especially on large flat expanses
520 of volcanic flow materials [*Watters, 1988; Bandert et al., 1997*]. Wrinkle ridges typically form
521 suites of near parallel structures (and occasionally orthogonal suites) formed over large regional
522 expanses. Locally within the AMA, wrinkle ridges occur as inversion structures formed by the
523 inversion of buried fractures due to post burial contraction [*DeShon et al., 2000*]; inversion
524 wrinkle ridges typically have straighter less sinuous trends reflecting the nature of their parent
525 fractures.

526 4.3.3 Tectonic fabrics

527 Tectonic fabrics comprise an assemblage of related structural elements that together
528 characterize a rock unit, as in the case of ribbon-tessera terrain [*Hansen & Willis, 1996, 1998;*
529 *Hansen, 2006*], or Artemis interior fabrics [*Bannister & Hansen, 2010*].

530 Ribbon-tessera fabric is characterized by orthogonally developed suites of ribbons, or
531 ribbon structures and folds. Ribbon structures record layer extension, whereas orthogonal fold
532 suites record layer contraction. Ribbon terrain is marked by parallel bright and dark lineaments
533 that represent alternating parallel ridges and troughs with typical wavelengths of 2 to 5 km
534 [*Hansen & Willis, 1996, 1998*]. Ribbon structures are commonly spatially associated with folds;
535 parallel fold crests and troughs typically trend at a high angle (generally 90°) to ribbon
536 lineaments. These ribbon-tessera folds defined parallel fold suites ranging in wavelength from
537 short (≤ 1 km), to intermediate, to long (order >10 km); longer wavelength folds host shorter-
538 wavelength folds, carrying them piggyback [*Hansen, 2006*]. Within the AMA we delineate the
539 trends of ribbon-tessera ribbons and folds. Ribbon trends parallel ribbon lineaments, whereas
540 fold trends parallel fold crests or troughs. In most cases short-, intermediate, and long-
541 wavelength folds display parallel local trends [*Hansen, 2006*]. Together, ribbons and folds
542 characterize ribbon-tessera terrain [*Hansen & Willis, 1996, 1998*]. Graben complexes, an
543 additional possible structural element of ribbon-tessera terrain, typically parallel ribbon trends.
544 Graben complexes are wider and shorter than ribbon structures, and thus display smaller length-
545 to-width ratios. Graben complexes that occur within ribbon-tessera terrain typically cut across
546 long-wavelength fold crests, which results in a lens-shape plan view [*Ghent & Hansen, 1999;*
547 *Hansen, 2006*]. *Bindschadler et al.* [1992] recognized ribbon, fold and graben structures within
548 tessera terrain. These workers describe described ribbon structures as “narrow troughs”, clearly
549 differentiating ribbon structures from generally parallel but morphologically different graben.
550 Some workers do not delineate ribbon and graben, which can lead to confusion with regard to the

551 temporal and kinematic evolution of ribbon-tessera fabric [e.g., *Gilmore et al.*, 1997, 1998],
552 whereas others simply map tessera terrain but do not identify the nature of the tessera fabric
553 structures, nor their trends [e.g., *Ivanov & Head*, 2011].

554 Collectively referred to as ribbon-tessera terrain, or ribbon terrain for short, this
555 distinctive composite tectonic fabric (e.g., ribbons and parallel graben, and orthogonal fold
556 suites) commonly marks tessera terrain. The composite fabric records a progressive change in the
557 rheological character of the deformed layer with time, from an early-formed thin layer to an
558 increasingly thicker layer with time and fabric development, likely a result of thermal history
559 [*Hansen & Willis*, 1998; *Ghent & Hansen*, 1999; *Brown & Grimm*, 1999; *Hansen*, 2006; *Ruiz*,
560 2007]. For a discussion of ribbon-terrain controversies, see *Gilmore et al.* [1998], *Hansen et al.*
561 [2000], and *Hansen* [2006].

562 Artemis hosts a second type of tectonic fabric within the AMA, as noted by *Bannister &*
563 *Hansen* [2010]. Artemis interior penetrative fabric represents closely spaced (0.5–1 km)
564 lineaments with slight gradation in radar brightness across strike. The lineaments are interpreted
565 in some cases as short-wavelength low-amplitude folds, and in other cases as fracture-like
566 structures; however, in many cases the fabric character is ambiguous given that the fabric
567 approaches the effective resolution [*Zimbleman*, 2001] of SAR. This distinctive tectonic fabric
568 has, to date, only been recognized within the interior of Artemis. The fabric may be analogous to
569 structural fabric development along terrestrial divergent plate boundaries [see *Bannister &*
570 *Hansen*, 2010]. Lineament trends are noted for Artemis interior tectonic fabric.

571 4.4 Map units

572 Map units are broadly defined in the following section. Readers should refer to the
573 description of map units for a complete description of all map units and specific material unit
574 characteristics (Plate 1).

575 In some cases, contacts between adjacent units are sharp and well defined, elsewhere
576 contacts are gradational, resulting from the low angle nature of individual contacts, as well as the
577 style of the units or terrains. For example, shield terrain (unit st), consists of a thin veil of
578 numerous *in situ* locally sourced deposits associated with individual shields a few km across
579 [*Guest et al.*, 1992; *Hansen*, 2005]; the location of the mapped contact could vary across 10s to
580 100 kilometers [e.g., *Hansen*, 2005; *Hansen*, 2009; *Hansen & Tharalson*, 2014]. The contacts of
581 basal terrain and overlying units also varies from sharp to gradational. Basal terrain cut by
582 fractures and later locally buried, typically displays sharp contacts marked by fracture truncation.
583 In other cases, lineaments appear in the overlying material, although the lineaments (fractures)
584 do not obviously cut the overlying material. In these cases, the overlying material is interpreted
585 to form a thin layer deposited on a basal unit cut by earlier-formed, now buried fractures. In
586 addition, the amount/character of fracture burial can also be gradational. Given these relations,
587 and the variation of fracture burial—from no burial to complete burial, the mapped contact
588 (viewed in planform), is typically shown as a gradational contact.

589 4.4.1 Terrain units (or lithodemic units)

590 The term “terrain” describes a texturally defined region, for example, a region where
591 tectonism imparted a surface with a penetrative deformation that disallows interpretation of the
592 original unit or units [*Wilhelms*, 1990]. Terrain units are examples of lithodemic units [*Hansen &*
593 *López*, 2018]. Characteristic texture could imply a shared history, such as a terrestrial tectono-
594 thermal history or an event that melds possibly previously unrelated rock units (any combination

595 of igneous, metamorphic, and sedimentary rocks) into gneissic terrain; no unique history is
596 inferred or required prior to the event(s) that melded potentially separate units into the textural
597 terrain (i.e., lithodemic unit). Events prior to terrain formation are unconstrained in time or
598 process unless specifically noted. Three general classes of terrain units occur across AMA:
599 ribbon-tessera terrain and related material, shield terrain and associate basal-shield terrain
600 transition, and fracture zone terrain.

601 *Ribbon-tessera terrain and related material* are delineated within AMA. Each of these
602 units includes the moniker ribbon-tessera terrain modified by the name of the host tessera region
603 (e.g., Ovda or Thetis ribbon tessera terrain, rtO and rtT, respectively), or a descriptive term such
604 as inlier of ribbon tessera (rti). These later terms are used for relatively small exposures or
605 occurrences in unnamed locations. Ribbon-tessera terrain units are differentiated using regional
606 location and structural trends. It is unclear how the various units are related to one another
607 temporally because interpretations of crosscutting relations are not unique. We also define units
608 associated with ribbon-tessera terrain: intratessera basin material unit itb [see *Banks & Hansen,*
609 *2000; Hansen, 2006*]. Similar to unit rt, unit itb is further divided based on location and/or
610 tessera terrain host (e.g., itbO, itbT, itbN).

611 Ribbon-tessera terrain typically displays orthogonal ribbon-fold tessera fabric [*Hansen &*
612 *Willis, 1998; Hansen, 2006*]. Fold wavelengths range from less than one kilometer—essentially
613 to the effective resolution [*Zimelman, 2001*] of SAR for folds, to tens of kilometers. Ribbon
614 wavelengths generally range from 2 to 5 km, although wavelengths locally occur to the effective
615 resolution of SAR. Intratessera basin material (unit itb) commonly fills intermediate- to long-
616 wavelength fold troughs. Unit itb also locally fills short-wavelength fold troughs, although such
617 deposits are not delineated here due to scale limitations. See *Hansen [2006]* for detailed geologic
618 maps of ribbon-tessera terrain within Ovda Regio; map relations, emergent temporal relations
619 and geological implications derived from that study are applicable to AMA ribbon-tessera
620 terrain.

621 Orthogonal ribbon-fold fabrics are the most common tessera fabric across AMA as they
622 are for ribbon-tessera terrain globally [*Hansen & Willis, 1996, 1998; Hansen & López, 2010*]. S-
623 C ribbon-tessera fabrics occur locally. S-C tessera fabric, first described by *Hansen [1992]* and
624 later by *Hansen & Willis [1996]*, shows a fabric asymmetry comprised of ductile and brittle
625 structures that together define coherent pictures of noncoaxial strain reflecting relative shear
626 displacement, similar to S-C fabrics within terrestrial ductile shear zones [e.g., *Berthé et al.,*
627 *1979*].

628 Both orthogonal ribbon-fold fabric and the S-C tessera fabric occur within ribbon-tessera
629 terrain preserved within crustal plateaus. S-C tessera fabric represents ductile shear zones in
630 central Ovda Regio, along its southern margin and along its eastern margin with Thetis Regio
631 [*Ghail, 2002; Tuckwell & Ghail, 2003; Kumar, 2005; Romeo et al., 2005*]. Orthogonal ribbon-
632 fold fabric and S-C tessera fabric could represent the deformation of the surface scum of huge
633 crystallizing lava ponds [*Hansen, 2006*]. Hawaii's lava lakes show dynamic flow fabrics of
634 extension, convergence, and strike-slip translation similar to terrestrial plate tectonic kinematic
635 patterns, presumably driven by convection within the lava lake. Similarly, Ovda's ancient lava
636 pond surface could record layer-parallel shortening and orthogonal extension (forming
637 orthogonal ribbon-fold tessera fabric), along with localized horizontal shear distributed over
638 several hundreds of kilometers (forming S-C tessera fabric) [*Hansen, 2006*].

639 *Local basal terrains*, or local basal terrain undivided, herein, is a term used to describe
640 surfaces that lie within locally low stratigraphic positions relative to adjacent map units. These

641 surfaces share suite(s) of tectonic structures that formed prior to the emplacement of adjacent
642 material; there is no implication of shared histories between spatially separated basal terrain units
643 across the AMA. However, it is possible that isolated (yet adjacent) basal terrain exposures may
644 represent temporally equivalent unconformity bound packages (i.e., allostratigraphic
645 surfaces/packages).

646 *Shield terrain* consists of thousands of individual shields and coalesced flow material,
647 referred to as “shield paint” for its apparent low viscosity during emplacement [Hansen, 2005;
648 see also Aubele, 1996]. Shield paint could be formed from any combination of lava flows, air-fall
649 deposits, or pyroclastic flows [Guest et al., 1992; Crumpler et al., 1997]. Shield terrain contains
650 material with an interpreted shared emplacement mechanism (represented by primary structures),
651 which differs from ribbon-tessera terrain whose elements include an interpreted shared
652 deformation history (represented by secondary structures).

653 Within the AMA, shield terrain material (unit st) is marked by distributed small (~1–10
654 km in diameter) shield edifices and associated local deposits. Unit st generally hosts a high
655 density of shields; although individual shields are not delineated due to map scale, and shield
656 density is difficult to robustly delineate [Hansen, 2005]. The contact of unit st with adjacent units
657 can be sharp or gradational over 10’s to 100’s of km as noted above. Unit st almost certainly
658 represents a time-transgressive unit across the AMA [e.g., Addington, 2001; Stofan et al., 2005],
659 comprised of thousands of local point-source eruptions that may represent point-source, *in situ*,
660 partial melting [Hansen, 2005]. This unit name is descriptive and does not imply temporal
661 equivalence.

662 Basal-shield transitional terrain (unit bst, southeastern AMA), marks a transition between
663 basal terrain and stratigraphically higher shield paint, delineated due to its transitional character
664 in which both the basal terrain and shield deposits are apparent.

665 Three lithodemic terrain units occur within the region including and encompassed by
666 Artemis Chasma: Artemis trough terrain (tAt) and Artemis tectonic terrains, tAa and tAb. The
667 latter correlate with units by the same names originally described by Bannister & Hansen [2010].
668 Artemis trough terrain—defined by trough parallel lineaments that variably correspond to normal
669 faults, thrust faults and folds crest/troughs—formed during the development of the Artemis
670 trough [Bannister & Hansen, 2010].

671 4.4.2 Mantling material

672 A mantling material occurs at high elevation locally blanketing ribbon-tessera terrain of
673 southern Ovda Regio. The mantling material occurs as both radar-bright and -dark regions
674 (shown as stipple pattern on host rtO) interpreted as elevation limited metal frost deposits
675 [Bleamaster & Hansen, 2005a], representing tellurium ‘snow’ [Pettengill et al., 1996; Kerr,
676 1996] or heavy metal precipitates of lead and bismuth [Schaefer & Fegley, 2004].

677 4.4.3 Material units

678 Material units are geologic materials interpreted to represent emplacement or deposition
679 as a coherent body or entity. Material units can be (1) lithostratigraphic units, which obey the
680 Law of Superposition and mark distinct temporal units (e.g., individual volcanic flows); (2)
681 bounded packages of similar emplacement character but formed at different times (e.g., impact
682 crater ejecta), and thus are not time equivalent; or (3) allostratigraphic, or unconformity-
683 bounded, composite units that cannot be robustly divided given available data and/or map scale
684 [Hansen & López, 2018].

685 *Artemis-related material* encompasses a suite of Artemis interior units fAa, fAb, and fAc
686 associated with tectonomagmatic features [Bannister & Hansen, 2010] and Artemis flows
687 undivided, unit Afu. Unit Afu is the most widely distributed material related to the Artemis
688 superstructure [Hansen & Olive, 2010]. Unit fAu, characterized by low-backscatter and low
689 RSM slope extends well beyond Artemis Chasma, covering much of southern AMA; unit fAu
690 both covers, and is locally cut by, the ~12,000 km diameter suite of Artemis-radial lineaments
691 [Hansen & Olive, 2010], interpreted as source structures for unit fAu material. Unit fAu is cut by
692 the ~13,000 km diameter suite of wrinkle ridges concentric to Artemis trough, which record late
693 collapse of the Artemis superplume [Hansen & Olive, 2010].

694 *Undivided flow material* includes three units: unit fchu (chasmata flow material
695 undivided), unit flu (localized lowland flows undivided), and unit fu (flows undivided). Unit fchu
696 is spatially associated with the regional fracture zone/corona-chasma system that cuts AMA from
697 east to west, occurring generally north of Artemis Chasma. Unit fchu shares a gradational contact
698 with unit fAu; the two units are delineated on the basis of spatial location, with unit fchu
699 occurring within the fracture zone regions. This unit likely includes a host of materials including
700 material emplaced prior to fracture zone development (which could include unit Afu), and local
701 flows contemporaneous with and genetically associated with fracture zone evolution. Units flu
702 and fu are characterized by generally low radar backscatter, low-RMS slope; unit flu occurs in
703 local topographic lows, whereas unit fu need not be topographically localized. None of these
704 units represent coherent time-specific lithostratigraphic units across AMA.

705 *Tholus, mons, and fracture fed flow material* are, as the name implies, material units
706 variably associated with tholus, mons, or fractures. Each unit show spatially limited extent
707 consistent with a genetic relationship to individual geomorphic features, and the unit name
708 includes the associated feature (e.g., fG, Gauri Mons flow material; fMh, Mahuea Tholus flow
709 material; fH Henwen Fluctus flow material; fLS, Lo Shen Valles flow material). Specific
710 characteristics are noted in map unit descriptions. In contrast to the other units, unit ff, flows
711 from fractures, is a descriptive unit—flows fed from fractures—it is not meant as a temporally
712 correlative unit. Unit ff material variably occurs as bright to dark on SAR images with lobate to
713 digitate flow fronts, channels, levees, breached levees, and well-preserved features indicative of
714 flow direction.

715 *Corona-related material and chasmata flow material* comprise the largest number of
716 units. Most are corona-related deposits—the majority of which are spatially associated with
717 individual coronae as indicated by the unit name (e.g., fAra, Aramaiti Corona flow a; fCe, Ceres
718 Corona flow material). Individual characteristics are noted in map unit descriptions (Plate 1).
719 Some coronae have more than one unit delineated; typically, such units are noted with a, b, c,
720 rather than 1, 2, 3. Numerical notation infers temporal constraints, which are typically lacking. In
721 some cases, specific corona flows define more proximal, or more distal facies. Location does not
722 carry robust temporal implications, given that distal and proximal facies could develop at
723 different times possibly related to corona evolution stages [e.g., Smrekar & Stofan, 1997, 1999;
724 McGovern et al., 2015]. We cannot independently and robustly determine the relative age of
725 flows given the currently available data. It is possible that flow facies formed time-
726 transgressively over the evolution of the host corona. We also map two units not defined as
727 coronae-specific, but rather that occur within many coronae—unit cc (corona center) and unit cif
728 (corona interior flow material). Both units occur in the center of coronae and each likely formed
729 relatively late during the formation of their host corona. Unit cc is typically radar-dark and may

730 include many small shields; unit cif typically displays digitate to lobate flow structures. Both
731 units are descriptive with no temporal equivalence implications across the AMA.

732 Material unit fcha (chasmata flow material a) is moderately bright on SAR images and
733 with digitate flow fronts, and local shield-type edifices; this unit is only rarely cut by secondary
734 structures, and is interpreted as comprised of relatively late, generally confined, flows associated
735 with formation of the Kuanja, Ralk-umgu, and Vir-ava Chasmata system.

736 4.4.4 Crater material

737 The AMA includes three regional distributed crater material units (units cfl, cf, and cu).
738 These units are time-transgressive having formed in association with individual impact craters
739 and not as lithostratigraphic packages. Unit cfl represents low viscosity, gently emplaced
740 material that locally flood the lowest portions of individual impact crater basins following, and
741 unrelated to, impact crater formation [*Izenberg et al.*, 1994; *Herrick & Sharpton* 2000; *Herrick*
742 *& Rumpf*, 2011]. Unit cf represents impact melt or fluidized ejecta created by meteorite impact
743 associated with the formation of individual impact craters; exposures are typically small. Unit cu,
744 crater material undivided includes radar bright material associated with impact crater formation
745 including crater ejecta and interior deposits.

746 Units cfM (Markham crater flow material) and cfAd (Addams crater flow material)
747 represent flows formed as a result of bolide impact associated with Markham and Addams
748 craters, respectively. The flows could be impact related, fluidized ejecta, or represent tapping of
749 pre-existing subsurface magma.

750 4.5 Tectonic structural suites

751 Tectonic (or secondary) structures form after the emplacement of a host material unit.
752 Suites of tectonic structures define local and regional patterns that collectively record a shared
753 deformation history and provide clues to operative tectonic or tectonomagmatic processes. We
754 use the terms local and regional tectonic suites to delineate different scales of tectonic suites.

755 4.5.1 Local tectonic suites

756 Local structural suites are spatially or geometrically associated with specific features
757 such as coronae or montes. Their timing likely corresponds to the formation, or stages of
758 formation, of the features with which they are associated, recognizing that feature development
759 could have been time-transgressive. These suites can be comprised of radial fractures (dikes at
760 depth, graben, faults), or concentric fractures, or both. Locally folds suites form concentric to
761 some coronae. In cases where concentric folds occur, folds generally are developed in north-
762 trending portions of an overall corona-centric pattern, whereas concentric fractures develop
763 along the east-trending portions of the same overall corona-centric pattern (e.g., Copia Corona;
764 42.5 S/75.5 E). Within the AMA, coronae with radial fracture suites dominate; although some
765 coronae are marked by prominent suites of concentric structures and generally lack radial
766 fracture suites (e.g., Ohogetsu, Aramaiti, Cailleach, and Khotun Coronae). In some cases, local
767 fractures change trend away from the host structure and become parallel to regional trends,
768 reflecting changes in local to regional stress fields [*Ernst et al.*, 1995; *López et al.*, 2008]. For
769 example, fractures concentric to Nishtigri Corona (24.5 S/72 E), which are developed best along
770 ENE-trends, lose their concentric geometry away from Nishtigri Corona becoming parallel to the
771 trend of regional fracture zone structures. In the case of Makh Corona (48.7 S/ 85 E), radial
772 fractures become parallel to regional fracture zone fracture (NE-trending). Chasmata and/or

773 troughs also occur spatially associated with many coronae, likely genetically related to their host
774 features. Chasmata and ridges are developed concentric to individual coronae, as well as aligned
775 between coronae; in such cases these features broadly define corona-chasma chains. We infer no
776 collective temporal equivalence of local radial and concentric suites across the AMA. (Note:
777 local suites of radial or concentric structures are associated with individual features, but
778 collectively these tectonic suites can be part of fracture zones and corona-chasma chains).

779 4.5.2 Regional tectonic suites

780 Regional structural suites describe coherent patterns across larger areas, lacking specific
781 spatial or geometric correlation with individual features. We identify two suites of regional
782 tectonic structures clearly associated with large-scale features; one group of structural suites is
783 related to the formation of the Artemis superplume [Hansen & Olive, 2010], and the other group
784 is related to the fracture zones and corona-chasma chains. We also delineate three suites of
785 orientation-defined fractures: NW-trending fractures transect southwestern AMA; generally N-
786 trending fractures are developed in south-central and southeast AMA. Each of these suites occur
787 within large, but limited areas, and are not obviously associated with other fractures suites.

788 4.5.2.1 Artemis-related structural suites

789 Two distinct suites of structures define the Artemis superstructure: fractures that describe
790 a pattern radial to Artemis Chasma with an overall radial fracture diameter on the order of
791 12,000 km, and wrinkle ridges that define a huge regionally-developed suite concentric to
792 Artemis Chasma, with an overall suite diameter on the order of 13,000 km [Hansen & Olive,
793 2010; Hansen & López, 2018; see also Hansen, 2002; Bannister & Hansen, 2010]. The fracture
794 suite, here referred to as Artemis-radial fractures, broadly pre-dated formation of the wrinkle-
795 ridge suite, referred to here as Artemis-concentric wrinkle ridges.

796 *Artemis-radial fractures* define a suite of fractures radial to Artemis Chasma cuts unit in
797 both the AMA and the NMA (I-2467) (Figure 1). The nature of this suite (broadly defined to
798 include fractures, dikes, lineaments, pit chains, stopping troughs) is particularly well-preserved in
799 southeastern AMA (domain 4) because that this region is relatively free of other features.
800 Individual fractures can extend several hundred kilometers. On the map fractures locally may
801 appear to end where the fracture package intersects with local basal units or with ribbon-tessera
802 units, due to difficulty in tracing the fractures across these basal terrains. Such abrupt truncation
803 of the fractures is likely an artifact of mapping. Packages of fractures also locally ‘end’ abruptly
804 where the fractures are buried by younger deposits; elsewhere the character of the fractures
805 become muted, due to shallow burial. Collectively the fracture suite defines a coherent pattern of
806 radial fractures, with the locus sharing the same center as the locus of Artemis Chasma. Regional
807 patterns of fully exposed fractures delineate exposures of pre-fracture basal terrain. Shallowly
808 buried fractures mark transitional basal terrain and overlying thin cover material. Regions where
809 fractures end abruptly along trend indicate areas of relatively thick cover resulting in essentially
810 complete burial of the fractured basal terrain. Fractures trend perpendicular to local wrinkle
811 ridges, which collectively define the Artemis-concentric wrinkle ridge suite. Artemis-radial
812 fractures are interpreted as having served as feeders for Artemis-related flows (e.g., unit Afu),
813 which were, in turn, deformed by Artemis-concentric wrinkle ridges along with numerous other
814 pre-existing flows.

815 Some Artemis-radial fractures can be difficult to distinguish from fractures within the
816 fracture zone domain. In general, where fracture zones parallel the trend of the Artemis-radial

817 fracture suite, we designate the fractures as Artemis-radial fractures. Fracture zones mark regions
818 of more focused zones of fracture development, referred to herein as spokes, given their overall
819 radial geometry with respect to Artemis Chasma. In cases where the fracture zones are not
820 parallel to the Artemis-radial fractures it is clear that the fractures are instead fracture zone
821 fractures. This may be a moot point in that the fracture zones radial to Artemis may be broadly
822 related to the Artemis superplume, and as such, these more defined ‘spokes’ of radial
823 deformation, may simply mark a different expression of the Artemis-radial fracture suite. The
824 fracture zone spokes may also have formed after Artemis-radial fractures, or out-lasted the
825 evolution of the Artemis-radial fracture suite. Robust detailed temporal relations are
826 unconstrained.

827 *Artemis-concentric wrinkle ridges* define a suite of wrinkle ridges concentric to Artemis
828 Chasma. Wrinkle ridges define low sinuous spines spaced a few kilometers apart and up to a few
829 hundred kilometers long, recording low (<2%) layer contractional strain. Wrinkle ridges are
830 developed across much of AMA, with the most striking suite concentric to Artemis Chasma.
831 This wrinkle ridge suite, with a diameter on the order of 13,000 km (Figure 1), affects most of
832 AMA and NMA. Like the fractures, wrinkle ridges occur at a range of spacing, down to small-
833 scale wrinkle ridges too closely spaced to show on the AMA geologic map.

834 Wrinkle ridges are notably absent within exposures of ribbon-tessera terrain, even in
835 high-resolution images, although wrinkle ridges occur locally in intratessera basin material (unit
836 itb). Wrinkle ridges occur right up to the contact between ribbon-tessera terrain and surrounding
837 units, such as Afu and st. These relations indicate that ribbon-tessera terrain is not rheologically
838 amenable to wrinkle ridge formation (that is, it lacks a thin deformable layer), whereas the thin
839 shield-terrain veneer or unit Afu can readily form wrinkle ridges. Similarly, some exposures of
840 local basal terrain (unit blu) are cut by Artemis-radial fractures but lack wrinkle ridges; thus,
841 these units are not rheologically amenable to wrinkle ridge formation.

842 Wrinkle ridges are also absent, or mostly absent, along the fracture zone ‘spokes’
843 broadly radial to Artemis. The most striking example of this is the Diana-Dali arm, where
844 wrinkle ridges end abruptly to the south of Atahensik Corona in northern Zhibek and Nsomeka
845 Planitiae, and in southern Rusalka Planitia north of Miralaidji Corona. Wrinkle ridges are also
846 mostly absent within the fracture zones in southwestern and western AMA. It is unclear whether
847 this absence results because the fracture zones dominantly post-date wrinkle ridge suite
848 development, or if these spokes, which typically lie at slightly higher elevations than the
849 surrounding regions, are typically not buried by thin flows, and as such, not rheologically
850 amenable to the formation of wrinkle ridges. Both explanations are possible. Locally flows
851 associated with coronae in the Diana-Dali region appear to both predate (deformed by) and post-
852 date (bury) Artemis-concentric wrinkle ridges. Corona-flows located at the off-axis distal edges
853 of the fracture zones (e.g. southernmost Atahensik and Flidais Coronae and northernmost Sith
854 Corona).

855 Artemis-concentric wrinkle ridges also deform many flows associated with individual
856 coronae or montes, particularly in western and southwestern AMA (e.g., Marzyana, Khotun,
857 Cailleach, Makh and Copia Coronae and Kunapipi Mons). These relations provide clear evidence
858 that the deformed corona/mons-related flows predated formation of this huge wrinkle-ridge suite.
859 Some corona/mons-associated flows do not host wrinkle ridges. These relations might result
860 because the flows formed after the Artemis-concentric wrinkle-ridge forming event, or these
861 flows were rheologically not amenable to wrinkle ridge formation, possibly due to flow
862 thickness, internal flow structure, or composition. For example, most flows associated with

863 Kunapipi Mons (unit fKu) do not show clear development of wrinkle ridges, however, wrinkle
864 ridges clearly cut the distal, and presumably thinner, edges of these flows. More proximal flows
865 might be too thick to form wrinkle-ridges, or, alternatively, portions of the Kunapipi flows could
866 post-date formation of the Artemis-concentric wrinkle ridge suite. In any case, map relations
867 within AMA highlight the challenge of robustly determining temporal relations between flows
868 and regional deformation ‘events’, such as the formation of wrinkle ridges. Clearly the evolution
869 and construction of a volcanic feature like Kunapipi Mons, and the formation of a regional suite
870 of wrinkle ridges, with a diameter of 13,000 km, are both likely to be time-transgressive, and
871 plausibly each could last tens to hundreds of millions of years.

872 Wrinkle ridges formed by inversion occur within Rusalka Planitia [*DeShon et al., 2000*].
873 Orthogonal patterns of wrinkle ridges in Rusalka Planitia east of Nuahine Tessera are the result
874 of earlier formed Artemis-radial fractures, which were later buried; following burial the filled
875 fractures were closed resulting in inversion of the fracture fill material and the formation of
876 straight (as opposed to sinuous) wrinkle ridges along strike with parts of the fractures that were
877 not buried. Fracture closure and resulting inversion of the fill likely occurred synchronous with
878 the formation of Artemis-concentric wrinkle ridges, which, together with the inversion-formed
879 wrinkle ridges define a suite of orthogonal wrinkle ridges. But it is also possible that the
880 inversion event occurred after (or even before) concentric wrinkle ridge formation, although
881 synchronous formation would be geologically reasonable.

882 4.5.2.2 Fracture zone structural suites

883 Fracture zone structural suites collectively define domain 3. Lineaments within the
884 fracture zones represent a range of planar structures that are manifested as lineaments in map
885 view (e.g., fractures, dikes, pit chains, troughs, scarps, stoping troughs, hybrid structures).
886 Individual zones display different mixes of structural elements, and some include coronae. For
887 example, The Diana-Dali corona-chasma chain hosts numerous scarps and troughs (chasmata)
888 that either parallel the zone or are curvilinear associated with individual large coronae. In
889 contrast the fracture zone at about 7 o’clock with respect to Artemis Chasma is characterized by
890 extremely closely-spaced lineaments, lacking ridges, troughs, or coronae. The Vir-ava/Ralk-
891 umgu chasmata zone displays extremely closely-space lineaments marked by narrow topographic
892 troughs including pit chains, stoping troughs, or hybrid lineament, and hosts a single corona,
893 Inari Corona. Structural elements within individual fracture zones are likely genetically related,
894 and the zones might also be collectively genetically related.

895 We delineate a new type of structural element, here referred to as, hybrid lineaments,
896 within the fracture zones. The need for this delineation arose given that individual lineaments
897 change along trend, and the effective resolution of the SAR data does not always allow for robust
898 identification of the nature of the lineament. Hybrid lineaments, or hybrid structures, are the
899 epitome of tectonovolcanic features; they can change along trend from zones of *en echelon*
900 fractures, fractures, pit-chains, graben, leaky dikes, stoping troughs, and channels. Widths range
901 from <1 km to >5 km; lengths can exceed several 100 km. Lineament spacing ranges from 10’s
902 of kilometers to lineament overlapping, intersecting, or coalescing. Hybrid structures can form
903 along trend with other lineaments or result from reactivation of parts of different lineament
904 suites, resulting in a stepped surface pattern, locally forming channels. Hybrid lineaments
905 likely occur throughout much of the fracture zone domain; many lineaments mapped as fractures
906 could be hybrid lineaments. Although hybrid structures locally source flows, evidence of this is
907 quite rare. More noteworthy is a striking lack of evidence for associated surface flows. The

908 major role of hybrid lineaments appears to be the transfer of material from the surface to
909 depth (rather than from depth to the surface) as evidenced by widespread development of pit-
910 chains, and topographic troughs and the lack of evidence for local burial [*Hansen & López,*
911 2014b]. If these structures transferred a significant amount of material from depth to the surface
912 then we would expect to observe numerous examples of flooding/filling of troughs by surface
913 flows, burial of troughs, and abrupt truncation of trough lineaments due to burial. However, few
914 such examples exist. If surface eruption was a common occurrence, we would expect that earlier
915 formed structures would be buried and effectively erased from the surface record. However,
916 evidence for a rich history is preserved, consistent with transfer of material to the subsurface.
917 Hybrid structures both predate and postdate various flows, providing evidence of their dynamic
918 role in the extensive volcano-magmatic province of southern Aphrodite Terra. The subsurface
919 nature of these structure remains unknown (i.e. fault, dike, or stoping-dominated), however the
920 incredibly close spacing of the lineaments, the topographic character of steep-sided flat based
921 troughs, the lack of associated surface flows, and the development over 100's of km of wide and
922 1000's of km long collectively indicate that these structures are unlikely to be associated with
923 crustal extension (e.g. dikes and/or normal faults). We favor a stoping interpretation [*Hansen &*
924 *López, 2014a, 2014b, 2018; Tovar et al., 2015*]. Discussion of this topic is outside the limits of
925 the map description text.

926 4.6 Impact features

927 AMA hosts 124 impact craters, ranging from 2.7 to 92.2 km diameter (Table 1). Table 1
928 lists crater location, diameter, elevation, crater density, host material units, etc. Most of the
929 craters are included in existing Venus crater data bases [e.g., *Schaber et al., 1992; Herrick et al.,*
930 1997]. Each impact crater displays an interior, rim and ejecta deposit; about 33% also have
931 parabolic or halo deposits [e.g., *Izenberg et al., 1994*]. Impact craters with rim diameter <14 km
932 generally lack central peaks. Impact crater deposits are shown as unit cu, crater material
933 undivided, representing interior and ejecta deposits associated with local bolide impact. Each
934 impact crater formed during a unique spatial and temporally localized event; therefore,
935 composite unit cu is diachronous across the map area. Over 40% of the craters display radar-
936 smooth interiors, unit cf, interpreted as interior flood deposits that formed after, and unrelated to,
937 initial impact crater formation [*Izenberg et al., 1994; Phillips & Izenberg, 1995; Herrick &*
938 *Sharpton, 2000; Herrick & Rumpf, 2011*]. For small diameter craters, unit cf is not shown; for
939 very small diameter craters the presence of absence of interior fill cannot be confirmed. Crater
940 haloes are shown as a stippled pattern.

941 None of AMA's craters show obvious signs of embayment by flows that breach an
942 individual crater rim; however, this relation does not require that crater formation is the youngest
943 local geologic event. Detailed mapping of Venus impact craters using high-resolution digital
944 elevation models indicates that dark-floored craters with diameter >20 km have an average rim-
945 floor depth of 290 m and rim height (measured from rim to the adjacent surroundings) of 240 m,
946 less than bright-floored craters, indicating significant post-crater volcanic modification of radar-
947 dark floored craters [*Herrick & Sharpton, 2000; Herrick & Rumpf, 2011*]. Thus, dark-floored
948 craters likely predate, rather than post-date, the emplacement of at least some of the adjacent
949 units (see figure 3 of *Hansen, 2000*, for a possible mechanism). Geologic mapping of individual
950 craters using high-resolution DEMs [e.g., *Herrick & Rumpf, 2011*] has not been employed in the
951 construction of the AMA.

952 Temporal relations between craters and tectonic events can be difficult to robustly
953 constrain. If a crater lies between structural elements that comprise the local tectonic suite, such
954 as wrinkle ridges or spaced fractures, the relative timing of crater formation and tectonic activity
955 cannot be determined [*Hansen, 2000*]. Evidence for crater deformation (or lack thereof) is noted
956 in Table 1 in cases where information can be extracted from map relations. At least 22 craters
957 show clear evidence of deformation (and four craters show possible deformation) indicating that
958 at least these craters formed before local tectonic activity ceased. However, an apparent lack of
959 deformation is not a robust positive test for crater formation after local tectonic activity given the
960 spaced nature of tectonic deformation fabrics and the point location of individual craters (see
961 figure 3 of *Hansen, 2000*). In addition, craters with diameter ≤ 7 km are generally too small to be
962 able to robustly determine if the craters are deformed; 25 craters within AMA (20%) have a
963 diameter ≤ 7 km, and therefore cannot be used to evaluate the relative timing of tectonic activity.
964 At least 22% (possibly $>26\%$) of the AMA's craters with diameter >7 km are deformed. This
965 observation is notable given that the AMA lies fully outside the Beta-Alta-Themis (BAT) region,
966 which encompasses the area of Venus marked by the lowest crater density and highest
967 percentage of craters obviously modified by tectonic or volcanic activity [e.g., *Phillips &*
968 *Izenberg, 1995; Herrick & Sharpton, 2000; Hansen & Young, 2007*].

969 Specific geological events occurred *after* the formation of some impact craters, as
970 indicated by cross-cutting relations (Table 1). Craters Abigail, Chiyojo, Gilmore, Huang Daopo,
971 Khelifa, Shushan and Yokhtik appear to be cut by Artemis-radial fractures and/or Artemis-
972 concentric wrinkle ridges; thus, these craters formed prior to these the cessation of the Artemis
973 superplume [e.g. *Hansen & Olive, 2010*]. Craters Agrippina and Xiao Hong might also be cut by
974 Artemis superstructure-related fractures and/or wrinkle ridges, and therefore could also have
975 predated cessation of the Artemis superplume. In addition, the following craters appear to be cut
976 by fracture-zone or coronae-chain structures, and therefore they were likely emplaced broadly
977 prior to (or during) fracture zone terrain evolution: Austen, Langtry, Maltby, Pavlinka, Teura,
978 Winnemucca, Whitney, and Yonge. Langtry Crater displays a flooded interior, which is cut by
979 fracture zone structures; therefore, emplacement of the interior crater fill (which formed after the
980 impact crater itself) occurred prior to fracture zone evolution, or at least prior to the end of
981 fracture zone evolution. Austen crater is cut by fractures related to Atahensik Corona, thus
982 predating final formation of Atahensik. Craters Yonge, Whitney, Maltby, Winnemucca, and
983 Pavlinka predate adjacent fracture zone structures and or corona/chasma zones. In contrast,
984 O'Connor, Halle, Martinez and Warren Craters both cover and are cut by fracture
985 zone/corona/chasma structures, therefore these impact craters likely formed at some point during
986 the time-transgressive evolution of these tectonomagmatic zones. Twelve percent of craters large
987 enough to record geologic relations pre-date, or formed synchronously with, fracture zone
988 structures and/or coronae. This observation indicates the relative youth of the fracture zone
989 domain and is consistent with the possibility that this zone remains geologically active. A nearly
990 equal number of craters (11 %) cross-cut local fracture zone structures, an observation—coupled
991 with the previous observation—consistent with a relatively long geological history of the fracture
992 zone domain, broadly speaking.

993 Twenty-two craters locally cover or bury Artemis-related structures or fracture zone
994 structures, indicating that these craters formed after the waning of these events. Although many
995 of these craters have radar-rough (bright) interiors and halo deposits, consistent with relatively
996 young ages [e.g., *Izenberg et al., 1994*], at least ten display filled interior regions. These craters

997 record a history of early Artemis-structure formation, followed by impact crater formation,
998 following in turn by interior flooding of these individual craters.

999 Markham Crater and Addams Crater in the northeast and southwest AMA, respectively,
1000 display impressive outflow deposits. Both formed on regions marked by suites of concentric
1001 fractures on the flanks of coronae—Markham on the eastern flank of Seia Corona, Addams on
1002 the eastern flank of Triglava Corona. Both impact craters display radar smooth interiors, and
1003 both have possible haloes deposits that ‘mute’ adjacent wrinkle ridge structures; and in both
1004 cases, associated outflow deposits likely postdate formation of Artemis-concentric wrinkle
1005 ridges. Both impact craters also display butterfly ejecta deposits indicative of oblique impact
1006 [e.g., *Schultz*, 1992]; Markham resulted from impact from the southwest, whereas Addams
1007 Crater formed due to impact from the northwest. Both craters apparently formed after, or
1008 possibly in the late stages of, the formation of Artemis concentric wrinkle ridges, and hence
1009 after, or late during, the waning stages of the Artemis superplume. Both impact craters likely
1010 tapped into subsurface magma chambers associated with their respective coronae-related
1011 structures. Given the location of these impact craters on the flanks of coronae, and their
1012 associated outflow material, it is likely that their radar smooth interiors also relate to their
1013 respective locations relative to their host coronae.

1014 The impact crater data and observations, independently and taken together with the
1015 observation that >40% of AMA craters show interior flooding, indicate that a significant number
1016 of AMA impact craters experienced notable geological events (i.e., interior fill emplacement)
1017 after their formation. These results are consistent with the results of analysis of high-resolution
1018 digital elevation model data of Venus impact craters, that reveal significant geologic
1019 modification of numerous impact craters [*Herrick & Rumpf*, 2011]. These results are contrary to
1020 initial surveys of the Venus crater population conducted using NASA Magellan data, used to
1021 suggest that only a few percent of Venus craters were deformed or embayed by volcanic material
1022 [*Schaber et al.*, 1992; *Phillips et al.*, 1992; *Herrick & Phillips*, 1994; *Strom et al.*, 1994; *Collins*
1023 *et al.*, 1999]. These new data, along with the *Herrick and Rumpf* [2011] study are difficult to
1024 accommodate within the context of catastrophic resurfacing models, or with any resurfacing
1025 models that require the vast majority of Venus impact craters to mark the top of the stratigraphic
1026 column [e.g., *Turcotte*, 1993; *Strom et al.*, 1994; *Solomatov & Moresi*, 1996; *Turcotte et al.*,
1027 1999; *Basilevsky & Head*, 1998, 2000, 2002a, 2002b, 2006; *Basilevsky et al.*, 1997, 1999; *Reese*
1028 *et al.*, 2007; *Romeo & Turcotte*, 2010; *Romeo*, 2013; *Ivanov & Head*, 2015a, 2015b; *Kreslavsky*
1029 *et al.*, 2015]. Thus, impact crater relations within the AMA cast doubt on the conclusions of
1030 these studies. In addition to the data described herein, a growing number of studies similarly
1031 indicate that hypotheses of catastrophic resurfacing, or hypotheses that call for late formation of
1032 most impact craters on Venus are inconsistent with geologic relations and/or modeling [e.g.,
1033 *Guest & Stofan*, 1999; *Herrick & Sharpton*, 2000; *Hansen & Young*, 2007; *Hansen & López*,
1034 2010; *Hansen & Olive*, 2010; *Herrick & Rumpf*, 2011; *Bjornnes et al.*, 2012; *O’Rourke & Jun*
1035 *Korenaga*, 2014, 2015], and collectively challenge assumptions that the Venus crater population
1036 represents a limited, young, geologic time period.

1037 **5 Geologic History**

1038 The geologic history that emerges from the AMA is, broadly speaking, relatively simple,
1039 although a rich regional history emerges (Figure 3). An ancient era marked by formation of
1040 ribbon-tessera terrain and crustal plateaus (and perhaps basal terrain), predated time-
1041 transgressive evolution of the Artemis superstructure; Artemis superstructure formation was

1042 broadly followed by, more spatially focused, evolution of the fracture zone domain marked by
1043 fracture zones and corona-chasma chains. Fracture zone and corona-chasma chain evolution
1044 seems to have broadly outlasted Artemis superstructure evolution.

1045 The broad regional history parallels the three major geological eras identified through
1046 structural-element mapping across the combined Niobe and Aphrodite map areas [*Hansen &*
1047 *López, 2018*]. The three eras—the ancient era, the Artemis Superstructure era and the fracture
1048 zone complex era—are discussed briefly below. Basal ribbon-tessera terrain units formed early
1049 across AMA and in a time-transgressive manner comprising the hallmark of the ancient era. Not
1050 all ribbon-tessera formed in one event, although ribbon-tessera terrain likely formed within an
1051 ancient geological era marked by specific geologic conditions, most notably an era marked by
1052 thin global lithosphere [*Phillips & Hansen, 1994, 1998; Bindschadler, 1995; Hansen et al.,*
1053 *2000; Hansen, 2006; Hansen & López, 2018*]. Composite yet local basal terrain (unit blu), which
1054 might mark areas between regions of ribbon-tessera terrain, could have formed before, during, or
1055 after the era during which ribbon-tessera terrain formed. Exposures of unit blu mark the lowest
1056 (local) exposed surfaces in each specific area of exposure; however, no data required that
1057 isolated exposures are geologically or temporally correlative. The exposures of unit blu are
1058 commonly cut by lineaments—mostly fractures, broadly defined. We do not recognize coherent
1059 patterns in these lineaments between exposures, unlike ribbon-tessera terrain, in which the
1060 structural fabrics are define by a unique and distinctive assemble of structural elements [e.g.,
1061 *Hansen & López, 2010*].

1062 Artemis, the hallmark of the Artemis Superstructure era, includes an interior high, a deep
1063 (~2 km) narrow (50–150 km) 2100-km-diameter trough (Artemis Chasma), outer rise (2400 km
1064 diameter), long-wavelength outer trough (5000 km diameter), radial dike swarm (12,000 km
1065 diameter), and concentric wrinkle ridges (13,000 km diameter). These features record
1066 progressive evolution of Artemis, as follows. (1) Initial doming and subsurface magma
1067 emplacement accompanied radial fracturing. (2) Fractures (subsurface dikes) propagated
1068 laterally, driven by magma buffering, producing dikes with widths and sizes independent of
1069 chamber size [*Parfitt & Head, 1993; Grosfils & Head, 1994; Ernst et al., 1995*]. Emplacement of
1070 lateral dikes in the constant driving pressure (magma buffered) produced dikes with sizes and
1071 widths that are very large and are independent of chamber size. (3) Dike-magma effusion fed
1072 local cover deposits (unit Afu), resulting in local burial of some radial fractures. (4) It is likely
1073 that an extensive region of the surface was uplifted as a result of superplume structure evolution.
1074 (5) Wrinkle ridges deformed the cover deposits (driven by coupling of convective mantle or
1075 plume flow to the lithosphere [e.g., *Phillips, 1990; Rosenblatt et al., 1994*]; and/or due to
1076 collapse of the huge regional uplift). (6) Late topographic collapse (and/or loading) resulted in
1077 formation of the broad outer trough (the trough might also record mantle flow). (7) Artemis
1078 Chasma and its interior region mark the decay of the Artemis superplume into a smaller (but still
1079 large) plume-type structure, resulting in regional localization of the Artemis interior and chasma
1080 [*Bannister & Hansen, 2010; Hansen & Olive, 2010*].

1081 The fracture zones and corona-chasma chains that define radial spokes relative to Artemis
1082 Chasma broadly post-date the formation of Artemis-radial fractures, and variably overlap in time
1083 with Artemis-concentric wrinkle ridge formation. In western AMA coronae mostly align along
1084 the fracture zones spokes, suggestive of a genetic relationship between coronae and fracture
1085 zones. We suggest that these features may have formed in a continuum with the Artemis
1086 superplume, perhaps forming in the waning stages of the superplume, and at the same time, or
1087 soon after, the Artemis plume came into existence. Evolution of the Diana-Dali corona-chasma

1088 chain outlasted the formation of Artemis-concentric wrinkle ridge suites as evidence by
1089 truncation/interruption of the wrinkle ridge trends across this zone. However, as noted, Artemis-
1090 concentric wrinkle ridges, which mark collapse of the Artemis superplume, cut some corona-
1091 sourced flows in Rusalka, Zhibek and Nsomeka Planitiae. The picture that emerges is one in
1092 which tectonism (deformation), and magmatic activity became spatially more focused with time.
1093 Initially the Artemis superplume resulted in uplift of a huge circumferential region coupled with
1094 formation of radial fractures with a footprint of at least 12,000 km diameter extending north into
1095 the NMA [Hansen & Olive, 2010; Hansen & López, 2018; López & Hansen, 2020]. Locally
1096 magma emerged from these radial fractures forming unit Afu. In some regions the radial
1097 fractures were reactivated, in some regions the fractures were not covered (similar to regions of
1098 ribbon-tessera terrain and local basal exposures which were not buried by these flows), and in
1099 some regions, the radial fractures were completely buried by these flows. Formation of the
1100 Artemis-concentric wrinkle ridge suite occurred broadly after formation of the Artemis-radial
1101 fractures, but wrinkle-ridge formation was outlasted in turn by more localized spokes of fracture-
1102 zone development. Some of the fracture zones were dominated by the formation of near-parallel
1103 fractures, whereas other zones were dominated by corona-mons formation. Elsewhere coroneae,
1104 chasmata and fractures developed in concert with one another along these fracture zones (e.g.,
1105 Diana-Dali). With time, the Artemis superplume decayed to the Artemis plume, and Artemis
1106 tectonic and volcanic activity became limited to the evolution of the interior of Artemis and
1107 Artemis Chasma [see Bannister & Hansen, 2010].

1108 The timing of shield terrain formation, unit st, is probably not the same across the AMA;
1109 however robust temporal constraints are not forthcoming. Locally Artemis-radial fractures cut
1110 shield terrain material; elsewhere shield terrain appears to cover Artemis-radial fractures. Shield
1111 terrain occurs in a broad band south of, and concentric to, Artemis Chasma. One possible mode
1112 of the formation of this unit is heating from below by the Artemis superplume, resulting in *in situ*
1113 partial melting of the overlying crust and emergence of point-source shield formation. It is
1114 possible that there is a spatial association, which might signal a genetic association, between
1115 ribbon-tessera terrain and shield terrain, but more focused research is required to evaluate this
1116 possibility.

1117 Mahuea Tholus, southwestern AMA, forms a unique volcanic feature given its isolation
1118 from other volcanic features and fracture zones. Moore *et al.* [1992] suggested that Mahuea
1119 Tholus flows might be highly siliceous based on the texture of its flow surfaces and terminations,
1120 and its isolated location and high topography character relative to the adjacent lowlands.
1121 Whatever the composition of Mahuea Tholus flows, distal unit fMhb is deformed by Artemis-
1122 concentric wrinkle ridges. Thus, Mahuea was at least partially active prior to the latest stages of
1123 the Artemis superplume. However, flow emplacement of unit fMha, located in a proximal
1124 location, either postdated formation of the Artemis-concentric wrinkle ridge suite, or is
1125 rheologically unsuited to host wrinkle ridges.

1126 The youngest regional-scale geological provinces and/or events within the AMA seem to
1127 be continued evolution of the Diana-Dali corona-chasma chain, and the Vir-ava/Ralk-umgu
1128 chasma zone including Inari Corona. Both zones, which are generally along strike with one
1129 another, extend ~2000 km in width and over 6000 km in length, and collectively define a zone
1130 marked by extensive tectonomagmatic activity. The Diana-Dali corona-chasma chain extends
1131 eastward to volcanic rise Atla Regio, which represents the surface expression of a large
1132 contemporary mantle plume [Smrekar & Phillips, 1991; Hansen *et al.*, 1997; Smrekar *et al.*,
1133 1997]. Atla Regio displays other tectonomagmatic fracture zones including Ganis Chasma, and

1134 the Hecate and Parga chasma-corona chains. Tectonic and magmatic activity along each of these
1135 spokes is likely genetically related to Atla Regio, and thus of similarly young age [*Hansen,*
1136 2018]. The Diana-Dali zone is dominated by large coronae, yet this region is also affected by a
1137 pervasively developed fracture zone. Coronae within the Diana-Dali zone may have sourced
1138 early surface flows (?), or not; but more recent activity appears to have been tectonic in nature,
1139 marked by the development of radial and concentric fractures, and fractures parallel to the
1140 regional trend of the zone. Fractures (broadly defined) and hybrid structures characterize the Vir-
1141 ava/Ralk-umgu chasmata zone; fracture-fed flows are relatively rare, or rarely preserved,
1142 occurring mostly along the edges of zones of pervasive fracture development; the region is
1143 characterized by pervasively developed fractures broadly parallel to the regional trend of the host
1144 zone. As noted, the general lack of young surface flows across the Diana-Dali and Vir-ava/Ralk-
1145 umgu chasma zones, is consistent with the development of topographically high and thin
1146 lithosphere [*Rosenblatt et al., 1994; McGovern et al., 2015*].

1147 **6 Conclusions**

1148 We conclude with a summary of a few first-order observations and/or geologic
1149 implications that emerge from the AMA geologic map.

1150 1. Coherent patterns across the AMA define broad geologic domains, and broad
1151 cross-cutting temporal relationships, illustrating the evolution of this portion of Venus'
1152 surface through time. These patterns were initially recognized through structural element
1153 mapping [*Hansen & López, 2018*], but the AMA geologic map further highlights these
1154 patterns, and adds important constraints and details. The three tectonic domains include, from
1155 oldest to youngest: 1) Ancient era ribbon-tessera terrain (including intratessera basin
1156 material) in both crustal plateaus and lowland inliers, and locally developed basal terrain. 2)
1157 Geologic units and structures associated with the development of the Artemis superstructure,
1158 including Artemis-radial fractures and -concentric wrinkle ridge suites, and Artemis-related
1159 flows (undivided); the later likely emerged to the surface via radial fractures prior to the
1160 formation of the wrinkle-ridge suite, which deforms the flows. Several material units
1161 associated with individual coronae or montes are also deformed by the extensive suite of
1162 Artemis-concentric wrinkle ridges (but not the Artemis-radial fracture suite). Collectively
1163 these relations indicate that flows sourced from localized features were emplaced (at least in
1164 part) prior to the final evolution of this regionally-developed Artemis-concentric wrinkle-
1165 ridge suite. Thus, the evolution of the coronae and montes overlapped with, but broadly
1166 outlasted the evolution of the Artemis superstructure (see below). Emplacement of lows that
1167 are not apparently deformed by the Artemis-concentric wrinkle-ridge suite could have post-
1168 dated wrinkle-ridge formation; however, such flows could also pre-date wrinkle-ridge
1169 formation, given that we must consider the possibility that individual flows, or parts of flows,
1170 were simply not rheologically amenable to wrinkle ridge development. 3) Development of
1171 the fracture zone terrain, including chains of coronae and chasmata, outlasted the cessation of
1172 the Artemis-concentric wrinkle-ridge suite. The fracture-zone terrain—marked by the Diana-
1173 Dali arm that extends east to volcanic rise Atla Regio, and fans into several arms to the west,
1174 clearly truncates (cross-cuts) the Artemis-concentric wrinkle ridge suite (Figure 3). Shield
1175 terrain within AMA (#5 below) formed prior to and/or early during the evolution of the
1176 Artemis superstructure given that shield terrain is both cut by, and locally covers, Artemis-
1177 radial fractures. The fractures could have been reactivated following shield terrain
1178 emplacement. Shield terrain is also generally cut by Artemis-concentric wrinkle ridges,

1179 indicating that shield terrain material was emplaced prior to development of this extensive
1180 wrinkle-ridge suite. These coherent regional patterns provide strong support that neither plate
1181 tectonic processes, nor ‘block processes’ marked by large-scale horizontal translations [e.g.
1182 *Byrne et al.*, 2018] occurred at any time as recorded in by geologic relations within the
1183 AMA.

1184 2. Given that Artemis-concentric wrinkle ridges cut numerous material units, many
1185 of which are flows that are clearly associated with individual coronae or mons, the
1186 identification of a singular plains unit/flow material characterized by wrinkle ridges is not a
1187 valid concept [e.g., *Basilevsky & Head*, 1998, 2000, 2002, 2006; *Ivanov & Head*, 2011, 2013,
1188 2015a, 2015b; *Head*, 2014]. These relations further call into question the global stratigraphy
1189 hypothesis given that the postulated ‘plains with wrinkle ridges’ (and variations on this
1190 naming) is not a valid material unit, yet forms a critical center piece of the global stratigraphy
1191 hypothesis [e.g., *Basilevsky & Head*, 1998, 2000, 2002, 2006; *Ivanov & Head*, 2011, 2013,
1192 2015a, 2015b; *Head*, 2014]. The concept of a coherent global stratigraphy through space and
1193 time is also a center piece to the hypothesis of (global) catastrophic resurfacing [*Bullock et*
1194 *al.*, 1993; *Strom et al.*, 1994; *Nimmo & McKenzie*, 1998; *Head*, 2014; *Ivanov & Head*,
1195 2015b]. Thus, the geologic relations documented within the AMA provide further evidence
1196 against the catastrophic resurfacing hypothesis. This evidence against the occurrence of
1197 catastrophic resurfacing of Venus should be considered with regard to geodynamic models of
1198 Venus that employ catastrophic resurfacing [e.g., *Armann & Tackley*, 2012; *Gillman &*
1199 *Tackley*, 2014; *Moore et al.*, 2017], and mission proposals with the stated goal to understand
1200 catastrophic resurfacing of Venus [e.g., *Smrekar et al.*, 2017; *Dyar & Smrekar*, 2018; *Dyar et*
1201 *al.*, 2018].

1202 3. Artemis-radial fractures and Artemis-concentric wrinkle ridges defined regional
1203 patterns relative to Artemis Chasma (12,000 km and ~13,000 km diameters, respectively)
1204 irrespective of the material units they define. These relations indicate that the wrinkle ridges
1205 are genetically related to an extremely large feature and not related to individual flows.

1206 4. The Diana-Dali corona-chasma fracture zone broadly cross cuts the Artemis-
1207 radial fractures and -concentric wrinkle ridge suites. These first-order relations provide
1208 robust temporal evidence that tectonic evolution of the Diana-Dali corona-chasma fracture
1209 zone outlasted ‘collapse’ of the Artemis superplume.

1210 5. Shield terrain, a unique style of volcanic unit first recognized and described by
1211 *Aubele* [1996] in Niobe Planitia and later characterized in detail by *Hansen* [2005], occurs as
1212 an extensive lithodemic terrain across the AMA in lowland locations. The evolution of this
1213 style of volcanism and the operative processes seem quite unique given the development of
1214 this type of terrain across huge regions, and yet the terrain is characterized by a thin surface
1215 layer marked by extremely local point-source volcanism. The volcanic and geodynamic
1216 significance of unit remains a mystery worth further study.

1217 6. Impact craters clearly formed time-transgressively across the AMA relative to
1218 each of the three major geologic eras noted above. Thus, there is no geologic evidence
1219 within the AMA that impact craters formed as the youngest ‘event’ across the AMA; nor do
1220 geologic relations require resurfacing of Venus. In fact, the range of temporal relations of
1221 impact craters provides evidence against catastrophic resurfacing hypotheses.

1222 7. The fracture zone domain, the youngest and most spatially-focused region of
1223 tectonomagmatic activity, post-dated formation of twelve percent of the impact craters large
1224 enough to record relative geologic relations. This observation is consistent with the

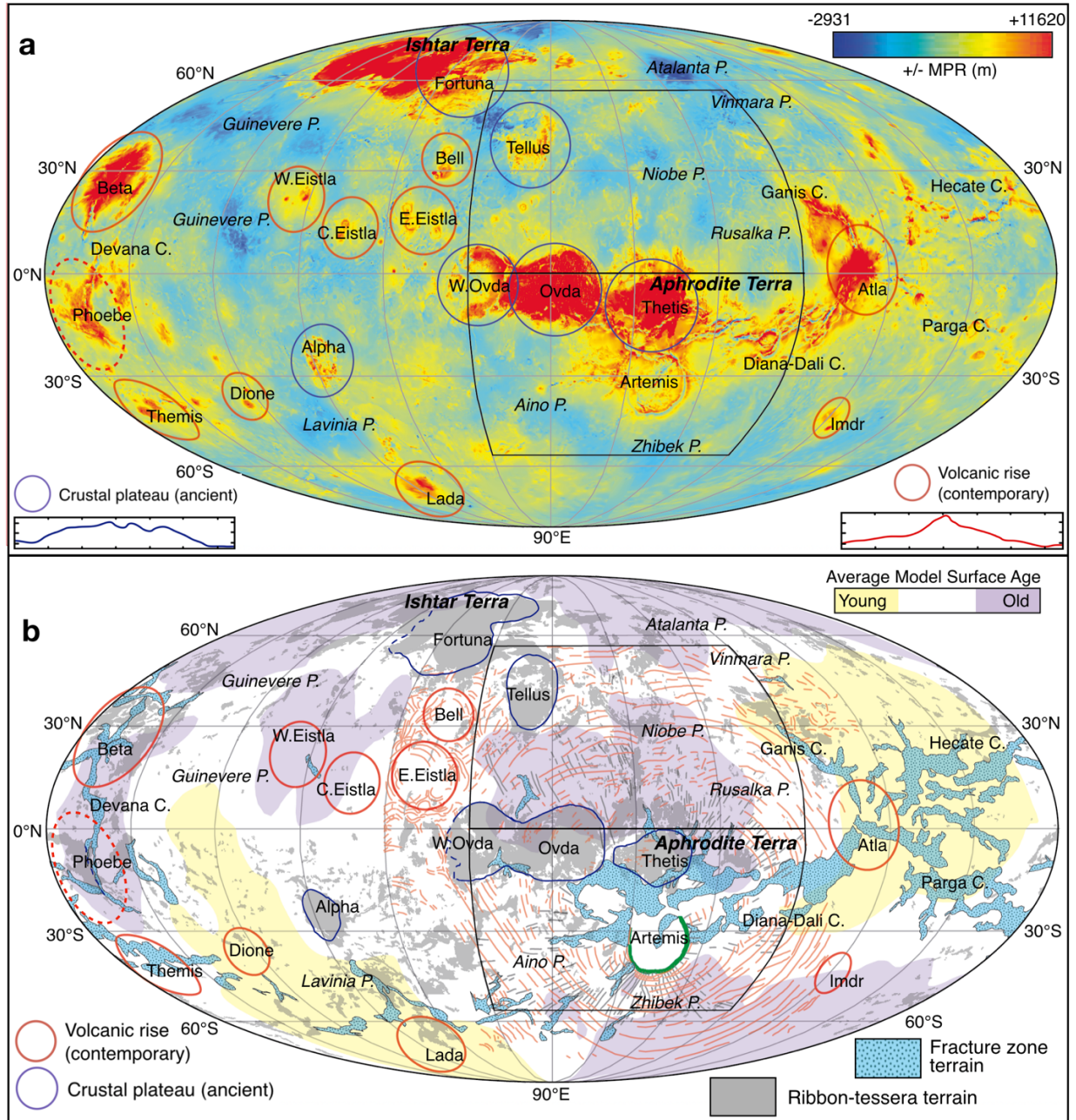
1225 possibility that the fracture zone domain could represent on-going geological activity.

1226 In summary, the most first-order observation that emerges from the AMA is the regional
1227 coherence of preserved geologic patterns, which provide a variable record of three relatively
1228 distinct geologic eras: the ancient era, the Artemis super structure era, and the youngest fracture
1229 zone terrain era. The first two eras are also variably recorded within the NMA [*Hansen & López,*
1230 2018]; all three eras can be extrapolated to the global scale, although the Artemis era is not
1231 strictly global as the Artemis superstructure covers about 30 percent of the planet surface
1232 [*Hansen, 2018*]. Geologic relations captured within the AMA illustrate the spatial and temporal
1233 relations of these three eras across time and space as described herein. Future geologic mapping,
1234 at a similar scale of the other four *IMap* areas east of the AMA—south and north of the equator
1235 (Helen Planitia [*I-2477*] and Guinevere Planitia [*I-2457*], respectively), and west of the AMA—
1236 south and north of the equator (Sedna Planitia [*I-2466*] and Lavinia Planitia [*I-2475*],
1237 respectively), will add important spatial and temporal information with regard to the evolution of
1238 these three geologic eras identified within the AMA. 1:10 M-scale mapping of these other
1239 regions, and the two polar 1:10 M cartographic sheets, might also lead to the identification of
1240 other geologic eras within the evolution of Earth’s sister planet Venus.

1241 **Acknowledgments and Data**

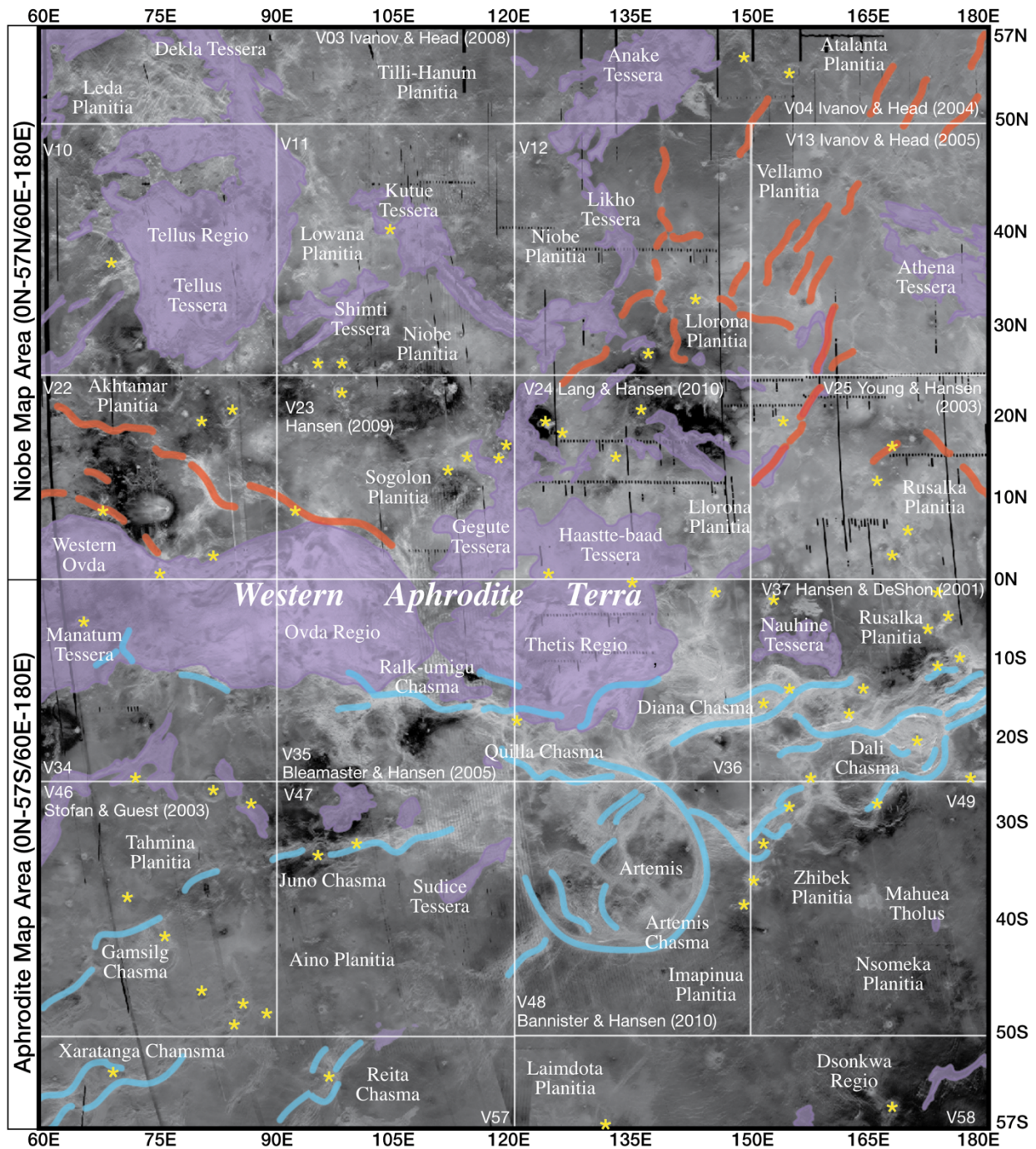
1242 Geologic mapping was supported by National Aeronautics and Space Administration (award
1243 NNX12AQ71G). NASA Magellan data are available via USGS Map a Planet website
1244 (<https://astrogeology.usgs.gov/tools/map-a-planet-2>). V. L. H. gratefully acknowledges support
1245 from the McKnight Foundation and the University of Minnesota. The authors have no financial
1246 conflicts of interests or other conflicts of interest with regard to this work.

1247
1248
1249
1250
1251



1252

1253 Figure 1. Mollweide projections of Venus; the NMA (north) and AMA (south) are shown as
 1254 polygons. (a) Altimetry: highlands, red; mesolands, yellow; lowlands, blues; Ishtar Terra and
 1255 Aphrodite Terra are composite highlands; highland features include crustal plateaus and volcanic
 1256 rises, and hybrid Phoebe Regio. Planitiae are indicated by ‘P.’, chasmata with ‘C.’ Topographic
 1257 profiles (Ovda Regio, 90°E; Beta Regio 23.6°E), ~6 km vertical, 3500 km horizontal. b) Global
 1258 distribution of: average model surface age provinces [Phillips & Izenberg, 1995; Hansen &
 1259 Young, 2007]; fracture zone terrain [‘rift’ of Price & Suppe, 1995]; ribbon-tessera terrain
 1260 [Hansen & López, 2010]; Artemis Chasma (green); trajectories of Artemis Chasma-radial
 1261 fractures (gray lines) and wrinkle ridges (faded red lines), including Artemis Chasma-concentric
 1262 wrinkle ridges and wrinkle ridges not concentric to Artemis [Hansen & Olive, 2010]. Labels as
 1263 in (a). Modified from Hansen [2018].



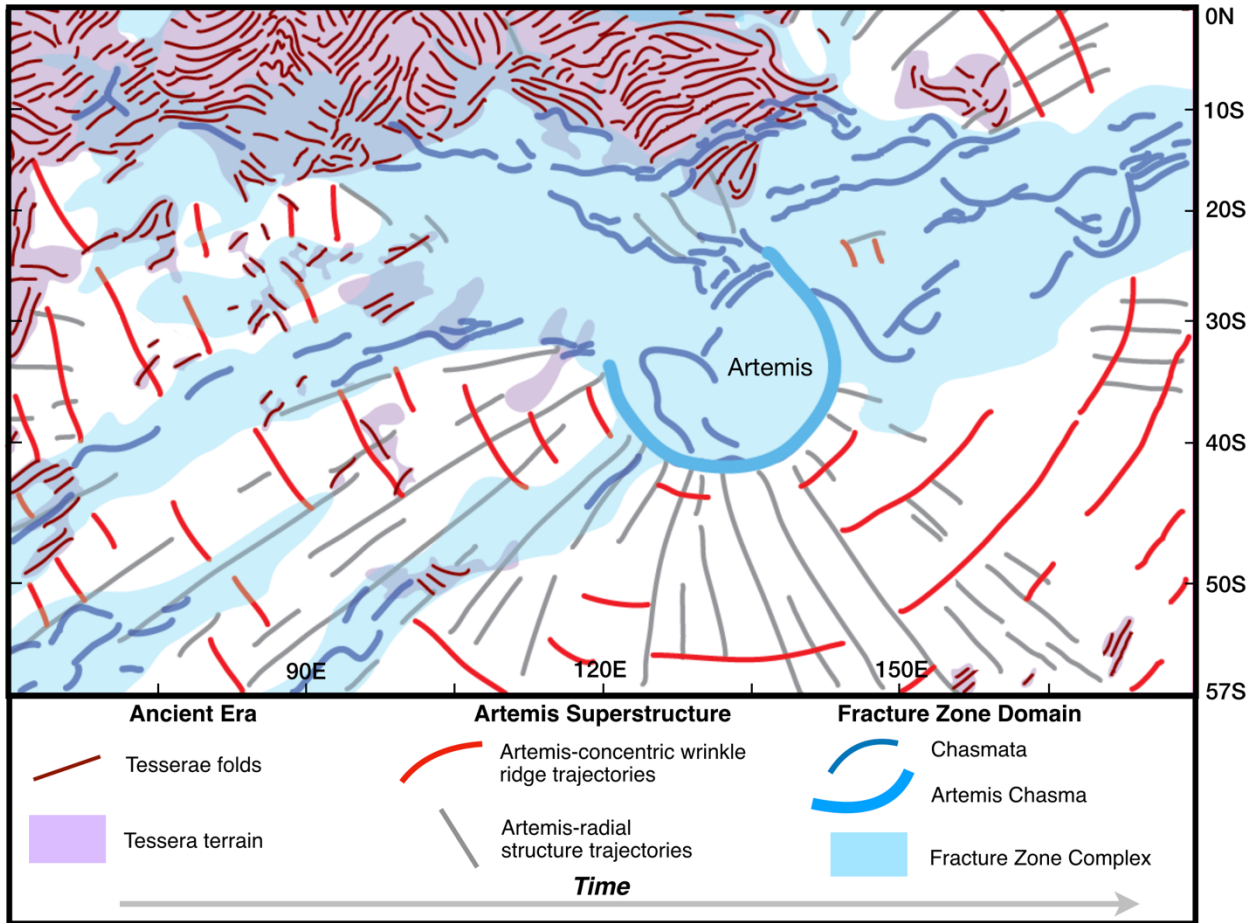
1264

1265

1266

1267

Figure 2. Mercator projection sketch map of Niobe and Aphrodite Map areas, SAR base with locations. Key: purple, tessera terrain; red lines, deformation belts; blue lines, chasmata; yellow stars, coronae; published VMap information in block text.



1268

1269 Figure 3. Mercator projection summary of the tectonic regimes within the AMA.

1270 **References**

- 1271 Addington, E. A. (2001). A stratigraphic study of small volcano clusters on Venus. *Icarus*, 149,
1272 16–36.
- 1273 Armann, M., & Tackley, P. J. (2012). Simulating the thermochemical magmatic and tectonic
1274 evolution of Venus's mantle and lithosphere: Two-dimensional models. *Journal of Geophysical*
1275 *Research: Planets*, 117(E12), doi:10.1029/2012JE004231
- 1276 Arvidson, R. E., Baker, V. R., Elachi, C., Saunders, R. S., and Wood, J. A. (1991), Magellan:
1277 Initial analysis of Venus Surface modification, *Science*, 252, 270–275.
- 1278 Arvidson, R. E., Greeley, R., Malin, M. C., Saunders, R. S., Izenberg, N., Plaut, J. J., Stofan, E.
1279 R., & Shepard, M.K. (1992). Surface modification of Venus as inferred from Magellan
1280 observation of plains. *Journal of Geophysical Research: Planets*, 97(E8), 13,303–13318.
- 1281 Aubele, J. (1996), Akkriva small shield plains; definition of a significant regional plains unit on
1282 Venus, LPSC, 27, 49–50.
- 1283 Baker, V. R., Komatsu, G., Gulick, V. C., & T. J. Parker (1997), Channels and valleys. In S. W.
1284 Bougher, D. M. Hunten, & R. J. Phillips (Eds.), *Venus II—Geology, geophysics, atmosphere, and*
1285 *solar wind environment* (Vol. 1, pp. 13395–13420). Tucson, AZ: University of Arizona Press.
- 1286 Baker, V. R., Komatsu, G., Parker, T. J., Gulick, V. C., Kargel, J. S. and Lewis, J. S. (1992).
1287 Channels and valleys on Venus—Preliminary analysis of Magellan data. *Journal of Geophysical*
1288 *Research: Planets*, 97(E8), 13421–13444.
- 1289 Baker, V. R., Hamilton, C. W., Burr, D. M., Gulick, V. C., Komatsu, G., Luo, W., Rice Jr, J. W.,
1290 & Rodriguez, J. A. P. (2015). Fluvial geomorphology on Earth-like planetary surfaces: a review.
1291 *Geomorphology*, 245, 149-182.
- 1292 Banerdt, W. B., McGill, G. E., & Zuber, M. T. (1997). Plains tectonics on Venus. In S. W.
1293 Bougher, D. M. Hunten, & R. J. Phillips (Eds.), *Venus II—Geology, geophysics, atmosphere, and*
1294 *solar wind environment* (Vol. 1, pp. 901–930). Tucson, AZ: University of Arizona Press.
- 1295 Banks, B. K., & Hansen, V. L. (2000). Relative timing of crustal plateau magmatism and
1296 tectonism at Tellus Regio, Venus. *Journal of Geophysical Research*, 105(E7), 17,655–17,667.
1297 <https://doi.org/10.1029/1999JE001205>
- 1298 Bannister, R. A., & Hansen, V. L. (2010). Geologic map of the Artemis quadrangle (V-48),
1299 Venus. U.S. Geological Survey Scientific Investigations Map 3099, 1:5M.
1300 <http://pubs.usgs.gov/sim/3099/>
- 1301 Basilevsky, A. T., & Head, J. W. (1998). The geologic history of Venus: A stratigraphic view.
1302 *Journal of Geophysical Research*, 103(E4), 8531–8544. <https://doi.org/10.1029/98JE00487>
- 1303 Basilevsky, A. T., & Head, J. W. (2000). Geologic units on Venus: Evidence for their global
1304 correlation. *Planetary and Space Science*, 48(1), 75–111. [https://doi.org/10.1016/S0032-](https://doi.org/10.1016/S0032-0633(99)00083-5)
1305 [0633\(99\)00083-5](https://doi.org/10.1016/S0032-0633(99)00083-5)
- 1306 Basilevsky, A. T., & Head, J. W. (2002a). On rates and styles of late volcanism and rifting on
1307 Venus. *Journal of Geophysical Research*, 107(E6), 5041. <https://doi.org/10.1029/2000JE001471>
- 1308 Basilevsky, A. T., & Head, J. W. (2002b). Venus: Timing and rates of geologic activity.
1309 *Geology*, 30, 1015–1018, doi:10.1130/0091-7613 (2002)030<1015:VTAROG>2.0.CO;2.

- 1310 Basilevsky, A. T., & Head, J. W. (2006). Impact craters on regional plains on Venus: Age
1311 relations with wrinkle ridges and implications for the geological evolution of Venus. *Journal of*
1312 *Geophysical Research*, *111*, E03006. <https://doi.org/10.1029/2005JE002473>
- 1313 Basilevsky, A.T., Head, J.W., Schaber, G.G., & Strom, R.G. (1997), The resurfacing history of
1314 Venus. In S. W. Bougher, D. M. Hunten, & R. J. Phillips (Eds.), *Venus II—Geology, geophysics,*
1315 *atmosphere, and solar wind environment* (Vol. 1, pp. 1047–1086). Tucson, AZ: University of
1316 Arizona Press.
- 1317 Basilevsky, A.T., Head, J.W., Ivanov, M.A., & Kryuchkov, V. P. (1999). Impact craters on
1318 geologic units of northern Venus: Implications for the duration of the transition from tessera to
1319 regional plains. *Geophysical Research Letters*, *26*, 2593–2596, doi:10.1029/1999GL008329.
- 1320 Berthé, D., Choukroune, P., & Jegouzo, P. (1979). Orthogneiss, mylonite and noncoaxial
1321 deformation of granite—The example of the South Armorican shear zone. *Journal of Structural*
1322 *Geology*, *1*, 31–42.
- 1323 Bindschadler, D. L. (1995). Magellan—A new view of Venus geology and geophysics. *Reviews*
1324 *in Geophysics*, *33*, 459–467. <https://doi.org/10.1029/95RG00281>
- 1325 Bindschadler, D. L., deCharon, A., Beratan, K. K., & Head, J. W. (1992b). Magellan
1326 observations of Alpha Regio: Implications for formation of complex ridged terrains on Venus.
1327 *Journal of Geophysical Research*, *97*(E8), 13,563–13,577. <https://doi.org/10.1029/92JE01332>
- 1328 Bjonnes, E. E., Hansen, V. L., James, B., & Swenson, J. B. (2012). Equilibrium resurfacing of
1329 Venus: Results from new Monte Carlo modeling and implications for Venus surface histories.
1330 *Icarus*, *217*(2), 451–461. <https://doi.org/10.1016/j.icarus.2011.03.033>
- 1331 Bleamaster, L. F., III, & Hansen, V. L. (2005). Geologic map of the Ovda Regio quadrangle (V-
1332 35), Venus. U.S. Geological Survey Geologic Investigation Series Map *I-2802*, 1:5M.
1333 <https://pubs.usgs.gov/imap/i2808/>
- 1334 Bullock, M. A., Grinspoon, D. H., & Head, J. W. (1993). Venus resurfacing rates: Constraints
1335 provided by 3-D Monte Carlo simulations. *Geophysical Research Letters*, *20*(19), 2147–2150.
1336 <https://doi.org/10.1029/93GL02505>
- 1337 Bussey, D. B.J., Sorenson, S. A., & Guest, J.E. (1995), Factors influencing the capability of lava
1338 to erode its substrate: Application to Venus. *Journal of Geophysical Research*, *100*(E8), 16,941–
1339 16,948.
- 1340 Butler, B. C. M., & Bell, J. D. (1988). *Interpretation of geological maps*. Essex. U.K.: Longman
1341 Science & Technical.
- 1342 Byrne, P. K., Ghail, R. C., Sengör, A. M. C., James, P. B., Klimczak, C. & Solomon, S. C.
1343 (2018), A Globally fragmented and mobile lithosphere on Venus. *LPI Contributions*, 2137.
- 1344 Campbell, B. A. (1999). Surface formation rates and impact crater densities on Venus. *Journal of*
1345 *Geophysical Research*, *104*(E9), 21,951–21,955. <https://doi.org/10.1029/1998JE000607>
- 1346 Campbell, B. A., & Campbell, D. B. (1992). Analysis of volcanic surface morphology on Venus
1347 from comparison of Arecibo, Magellan, and terrestrial airborne radar data. *Journal of*
1348 *Geophysical Research*, *105*(E10), 16,293–16,314.

- 1349 Campbell, B. A., Campbell, D. B., Morgan, G. A., Carter, L. M., Nolan, M. C., & Chandler, J. F.
 1350 (2015), Evidence of crater ejecta on Venus tessera terrain from Earth-based radar images. *Icarus*,
 1351 250, 123–130, <https://doi.org/10.1016/j.icarus.2014.11.025>
- 1352 Collins, G. C., Head, J. W., Basilevsky, A. T., & Ivanov, M. A. (1999). Evidence for rapid
 1353 regional plains emplacement on Venus from the population of volcanically embayed impact
 1354 craters. *Journal of Geophysical Research*, 104(E10), 24121–24139.
- 1355 Compton, R. R. (1985). *Geology in the field*. NY: John Wiley & Sons.
- 1356 Crumpler, L. S., Aubele, J. C., Senske, D. A., Keddie, T. D., Magee, K. P., & Head, J. W.
 1357 (1997). Volcanoes and centers of volcanism on Venus. In S. W. Bougher, D. M. Hunten, & R. J.
 1358 Phillips (Eds.), *Venus II—Geology, geophysics, atmosphere, and solar wind environment* (Vol. 1,
 1359 pp. 697–756). Tucson, AZ: University of Arizona Press.
- 1360 Cushing, G. E., Okubo, C. H., & Titus, T. N. (2015). Atypical pit craters on Mars. New insights
 1361 from THEMIS, CTX, and HiRISE observations. *Journal of Geophysical Research: Planets*, 120,
 1362 1023–1043. <https://doi.org/10.1002/2014JE004735>
- 1363 DeShon, H. R., Young, D. A., & Hansen, V. L. (2000). Geologic evolution of southern Rusalka
 1364 Planitia, Venus. *Journal of Geophysical Research*, 105, 6983–6995.
- 1365 Dyar, D., & Smrekar, S. E. (2018). Venus: Our misunderstood sister, In *AAS/Division for*
 1366 *Planetary Sciences Meeting Abstracts* (Vol. 50).
- 1367 Dyar, D., Smrekar, S. E., & Glaze, L. S. (2018). The case for Venus. *Physics Today*.
 1368 <https://doi.org/10.1063/PT.6.3.20180323a>
- 1369 Easton, R. M., Edwards, L. E., Orndorff, R. C., Duguet, M., & Ferrusqua-Villafranca, I. (2016).
 1370 North American commission on stratigraphic nomenclature North American Commission On
 1371 Stratigraphic Nomenclature Report 12—Revision of article 37, Lithodemic Units, of the North
 1372 American Stratigraphic Code. *Stratigraphy*, 13(3), 220–222.
- 1373 Easton, R. M., Jones, J. O., Lenz, A. C., Ferrusqua-Villafranca, I., Mancini, E. A., Wardlaw, B.
 1374 R., Edwards, L. E., & Pratt, B.R. (2005). North American commission on stratigraphic
 1375 nomenclature. *AAPG Bulletin*, 89(11), 1459–1464. <https://doi.org/10.1306/05230505015>
- 1376 Ernst, R. E., Head, J. W., Parfitt, E., Grosfils, E., & L. Wilson (1995). Giant radiating dyke
 1377 swarms on Earth and Venus. *Earth-Science Reviews*, 39(1-2), 1–58.
- 1378 Ferrill, D. A., Wyrick, D. Y., Morris, A. P., Sims, D. W., & Franklin, N. M. (2004). Dilational
 1379 fault slip and pit chain formation on Mars. *GSA Today*, 14(10), 4–12.
 1380 [https://doi.org/10.1130/1052-5173\(2004\)014<4:DFSAPC>2.0.CO;2](https://doi.org/10.1130/1052-5173(2004)014<4:DFSAPC>2.0.CO;2)
- 1381 Ford, J. P., & Plaut, J. J. (1993). Magellan image data. In J. P. Ford, et al. (Eds.), *Guide to*
 1382 *Magellan image interpretation, National Aeronautics and Space Administration Jet Propulsion*
 1383 *Laboratory Publication 93–24* (pp. 7–18). Pasadena, CA: NASA JPL.
- 1384 Ford, J. P., Plaut, J. J., Weitz, C. M., Farr, T. G., Senske, D. A., Stofan, E. R., et al. (1993b).
 1385 Guide to Magellan Image Interpretation. *National Aeronautics and Space Administration Jet*
 1386 *Propulsion Laboratory Publication, 93–24*, 148.
- 1387 Ghail, R. C. (2002). Structure and evolution of southeast Thetis Regio. *Journal of Geophysical*
 1388 *Research*, 107(E8), doi:[10.1029/2001JE001514](https://doi.org/10.1029/2001JE001514).

- 1389 Ghent, R., & Hansen, V. (1999). Structural and kinematic analysis of eastern Ovda Regio,
 1390 Venus: Implications for crustal plateau formation. *Icarus*, 139(1), 116–136.
 1391 <https://doi.org/10.1006/icar.1999.6085>
- 1392 Gilbert, G. K. (1886). Inculcation of the scientific method. *American Journal of Science*, 31,
 1393 284–299.
- 1394 Gillmann, C., & Tackley, P. (2014). Atmosphere/mantle coupling and feedbacks on Venus.
 1395 *Journal of Geophysical Research: Planets*, 119, 1189–1217.
 1396 <https://doi.org/10.1002/2013JE004505>
- 1397 Gilmore, M. S., Collins, G. C., Ivanov, M. A., Marinangeli, L., & Head, J. W. (1998). Style and
 1398 sequence of extensional structures in tessera terrain, Venus. *Journal of Geophysical Research*,
 1399 103(E7), 16,813–16,840. <https://doi.org/10.1029/98JE01322>
- 1400 Gilmore, M. S., Ivanov, M. A., Head, J. W., & Basilevsky, A. T. (1997). Duration of tessera
 1401 deformation on Venus. *Journal of Geophysical Research*, 102(E6), p.13357–13368.
- 1402 Gregg, T. K. P., & Greeley, R. (1993). Formation of venusian canali: Consideration of lava types
 1403 and their thermal behaviors. *Journal of Geophysical Research*, 98(E6), 10,873–10,882.
- 1404 Grindrod, P.M., & Guest, G. E. (2006), 1:1.5,000,000 Geological map of the Aglaonice region
 1405 on Venus. *Journal Maps*, 2:1, 103–117, doi:10.4113/jom.2006.57
- 1406 Grosfils, E. B., & Head, J. W. (1994). The global distribution of giant radiating dike swarms on
 1407 Venus: Implications for the global stress state. *Geophysical Research Letters*, 21(8), 701–704.
 1408 <https://doi.org/10.1029/94GL00592>
- 1409 Guest, J. E., Bulmer, M. H., Aubele, J., Beratan, K., Greeley, R., Head, J. W., Michaels, G.,
 1410 Weitz, C. & Wiles, C. (1992). Small volcanic edifices and volcanism in the plains of Venus.
 1411 *Journal of Geophysical Research: Planets*, 97(E10), 15949-15966.
- 1412 Guest, J. E., & Stofan, E. R. (1999). A new view of the stratigraphic history of Venus. *Icarus*,
 1413 139(1), 55–66. <https://doi.org/10.1006/icar.1999.6091>
- 1414 Hansen, V. L. (1992), Regional non-coaxial deformation on Venus—Evidence from western
 1415 Izapalotl Tessera, *LPSC XXIII*, 478–479.
- 1416 Hansen, V. L. (2000). Geologic mapping of tectonic planets. *Earth and Planetary Science*
 1417 *Letters*, 176(3-4), doi:10.1016/S0012-821X(00)00017-0
- 1418 Hansen, V. L. (2002). Artemis: Surface expression of a deep mantle plume on Venus. *Geological*
 1419 *Society of America Bulletin*, 114(7), 839–848. [https://doi.org/10.1130/0016-7606\(2002\)114<0839:ASEOAD>2.0.CO;2](https://doi.org/10.1130/0016-7606(2002)114<0839:ASEOAD>2.0.CO;2)
- 1420
- 1421 Hansen, V. L. (2005). Venus’s shield-terrain. *Geological Society of America Bulletin*, 117(5),
 1422 808–822. <https://doi.org/10.1130/B256060.1>
- 1423 Hansen, V. L. (2006). Geologic constraints on crustal plateau surface histories, Venus: The lava
 1424 pond and bolide impact hypotheses. *Journal of Geophysical Research*, 111, E11010.
 1425 <https://doi.org/10.1029/2006JE002714>
- 1426 Hansen, V. L. (2009). Geologic map of the Niobe Planitia Quadrangle (V-23), Venus. U.S.
 1427 Geological Survey Scientific Investigations Map 3025, 1:5M. <http://pubs.usgs.gov/sim/3025/>

- 1428 Hansen, V. L. (2018). Global tectonic evolution of Venus, from exogenic to endogenic over
1429 time, and implications for early Earth processes. *Philos. Trans. R. Soc.*, A376: 20170412.
1430 <https://doi.org/10.1098/rsta.2017.0412>
- 1431 Hansen, V. L., & DeShon, H. R. (2002). Geologic map of the Diana Chasma Quadrangle (V-37),
1432 Venus. U.S. Geological Survey Geologic Investigations Series I-27
- 1433 Hansen, V. L., & López, I. (2010). Venus records a rich early history. *Geology*, 38(4), 311–314.
1434 <https://doi.org/10.1130/G30587.1>
- 1435 Hansen, V. L., & López, I. (2014a). Southern Aphrodite fracture zone, Venus: Subsurface to
1436 surface volcano-tectonic connections, and a new mechanism for heat transfer. *Geological Society
1437 of America Abstracts with Programs*, 46(6), 505.
- 1438 Hansen, V. L., & López, I. (2014b). Hybrid fracture/dike/graben/pit-chain/canali structures on
1439 Venus: Dynamic interplay between surface and subsurface components of volcano-tectonic
1440 systems. *Geological Society of America Abstracts with Programs*, 46(6), 563.
- 1441 Hansen V. L., & López, I. (2018). Mapping of geologic structures in the Niobe-Aphrodite map
1442 area of Venus: unraveling the history of tectonic regime change. *Journal of Geophysical
1443 Research: Planets*, <https://doi.org/10.1029/2018JE005566>
- 1444 Hansen, V. L., & Olive, A. (2010). Artemis, Venus: The largest tectonomagmatic feature in the
1445 solar system? *Geology*, 38(5), 467–470. <https://doi.org/10.1130/G30643.1>
- 1446 Hansen, V. L. & Phillips, R. J. (1993). Tectonics and volcanism of Eastern Aphrodite Terra: No
1447 subduction, no spreading. *Science*, 260, 526–30.
- 1448 Hansen V. L., & Tharalson, E. R. (2014). Geologic Map of the Agnesi Quadrangle (V-45),
1449 Venus, U. S. Geological Survey, SIM 3250, 1:5M, <https://pubs.er.usgs.gov/publication/sim3250>
- 1450 Hansen, V. L., & Willis, J. J. (1996). Structural analysis of a sampling of tesserae: Implications
1451 for Venus geodynamics. *Icarus*, 123(2), 296–312. <https://doi.org/10.1006/icar.1996.0159>
- 1452 Hansen, V. L., & Willis, J. J. (1998). Ribbon terrain formation, southwestern Fortuna Tessera,
1453 Venus: Implications for lithosphere evolution. *Icarus*, 132(2), 321–343.
1454 <https://doi.org/10.1006/icar.1998.5897>
- 1455 Hansen, V. L., & Willis, J. J. (1998). Ribbon terrain formation, southwestern Fortuna Tessera,
1456 Venus: Implications for lithosphere evolution. *Icarus*, 132(2), 321–343.
1457 <https://doi.org/10.1006/icar.1998.5897>
- 1458 Hansen, V. L., & Young, D. A. (2007). Venus evolution: A synthesis. In M. Cloos, W. D.
1459 Carlson, M. C. Gilbert, J. G. Liou, & S. S. Sorensen (Eds.), *Convergent Marg Terranes and
1460 associated regions: A tribute to W.G. Ernst*, *Geological Society of America Special Paper* (Vol.
1461 419, pp. 255–273). Denver: Geological Society of America.
1462 [https://doi.org/10.1130/2006.2419\(13\)](https://doi.org/10.1130/2006.2419(13))
- 1463 Hansen, V. L., Phillips, R. J., Willis, J. J., & Ghent, R. R. (2000). Structures in tessera terrain,
1464 Venus: Issues and answers. *Journal of Geophysical Research*, 105(E2), 4135–4152.
1465 <https://doi.org/10.1029/1999JE001137>

- 1466 Hansen, V. L., Willis, J. J., & Banerdt, W. B. (1997). Tectonic overview and synthesis. In S. W.
1467 Bougher, D. M. Hunten, & R. J. Phillips (Eds.), *Venus II—Geology, geophysics, atmosphere, and*
1468 *solar wind environment* (Vol. 1, pp. 797–844). Tucson, AZ: University of Arizona Press.
- 1469 Head, J. W. (2014). The geologic evolution of Venus: Insights into Earth history. *Geology*,
1470 42(1), 95–96. <https://doi.org/10.1130/focus012014.1>
- 1471 Head, J. W., & Wilson, L. (1991). Absence of large shield volcanoes and caldera on the Moon:
1472 Consequence of magma transport phenomena?. *Geophysical Research Letters*, 18, 2121–2124.
- 1473 Herrick, R. R., & Phillips, R. J. (1994). Implications of a global survey of Venusian impact
1474 craters. *Icarus*, 111(2), 387–416. <https://doi.org/10.1006/icar.1994.1152>
- 1475 Herrick, R. R., & Rumpf, M. E. (2011). Post impact modification by volcanic or tectonic
1476 processes as the rule, not the exception, for Venusian craters. *Journal of Geophysical Research*,
1477 116, E02004. <https://doi.org/10.1029/2010JE003722>
- 1478 Herrick, R. R., & Sharpton, V. L. (2000). Implications from stereo-derived topography of
1479 Venusian impact craters. *Journal of Geophysical Research*, 105(E8), 20,245–20,262.
1480 <https://doi.org/10.1029/1999JE001225>
- 1481 Herrick, R. R., Sharpton, V. L., Malin, M. C., Lyons, S. N., & Feely, K. (1997). Morphology and
1482 morphometry of impact craters. In S. W. Bougher, D. M. Hunten, & R. J. Phillips (Eds.), *Venus*
1483 *II—Geology, geophysics, atmosphere, and solar wind environment* (Vol. 1, pp. 1015–1046).
1484 Tucson, AZ: University of Arizona Press.
- 1485 Ivanov, M. A., & Head, J. W. (2011). Global geological map of Venus. *Planetary and Space*
1486 *Science*, 59(13), 1559–1600. <https://doi.org/10.1016/j.pss.2011.07.008>
- 1487 Ivanov, M. A., & Head, J. W. (2015a). The history of tectonism on Venus: A stratigraphic
1488 analysis. *Planetary and Space Science*, 113, 10–32.
- 1489 Ivanov, M. A., & Head, J. W. (2015b). Volcanically embayed craters on Venus: Testing the
1490 catastrophic and equilibrium resurfacing models. *Planetary and Space Science*, 106, 116–121.
1491 <https://doi.org/10.1016/j.pss.2014.12.004>
- 1492 Izenberg, N. R., Arvidson, R. E., & Phillips, R. J. (1994). Impact crater degradation on Venusian
1493 plains. *Geophysical Research Letters*, 21, 289–292.
- 1494 Jones, A. P., & Pickering, K. T. (2003). Evidence for aqueous fluid-sediment transport and
1495 erosional processes on Venus. *Journal Geological Society of London*, 160, 319–327.
- 1496 Kerr, R. A. (1996). Does tellurium frost Venus’s highlands?. *Science*, 271, 28–29.
- 1497 Kirk, R., Soderblom, L., & Lee, L. (1992). Enhanced visualization for interpretation of
1498 Magellan radar data—Supplement to the Magellan special issue. *Journal of Geophysical*
1499 *Research*, 97, 16371–16380.
- 1500 Kreslavsky, M. A., Ivanov, M. A., & Head, J. W. (2015). The resurfacing history of Venus:
1501 Constraints from buffered crater densities. *Icarus*, 250, 438–450.
- 1502 Komatsu, G., & Baker, V. R. (1994), Meander properties of venusian channels. *Geology*, 22, 67–
1503 70.
- 1504 Kumar, P. S. (2005). An alternative kinematic interpretation of Thetis Boundary Shear Zone,
1505 Venus. *Journal of Geophysical Research*, 110(E070010), doi:[10.1029/2004JE002387](https://doi.org/10.1029/2004JE002387).

- 1506 Lang, N. P., & Hansen, V. L. (2010). Geologic map of the Greenaway quadrangle (V-24),
1507 Venus. U.S. Geological Survey Scientific Investigations Map 3089, 1:5M.
1508 <http://pubs.usgs.gov/sim/3089/>
- 1509 Lang, N. P., & Hansen, V. L. (2006). Venusian channel formation as a subsurface process.
1510 *Journal of Geophysical Research*, 111, <https://doi.org/10.1029/2005JE002629>
- 1511 López, I., & Hansen, V. L. (2018). Geographic information system of structural elements in the
1512 Niobe-Aphrodite map area of Venus: A tool for structural and geologic analysis. [data set].
1513 Zenodo. <http://doi.org/10.5281/zenodo.1256009>
- 1514 López, I., Lillo, J., & Hansen, V. L. (2008). Regional fracture patterns around volcanoes:
1515 Possible evidence for volcanic spreading on Venus. *Icarus*, 195(2), 523–536.
1516 <https://doi.org/10.1016/j.icarus.2007.12.026>
- 1517 Maltman, A. (1990). *Geological maps: An introduction* (p. 184). Buckingham U.K.: Open
1518 University Press. <https://doi.org/10.1007/978-1-4684-6662-1>
- 1519 McGovern, P. J., Grosfils, E. B., Galgana, G. A., Morgan, J. K., Rumpf, M. E., Smith, J. R., &
1520 Zimbelman, J. R. (2015). Lithospheric flexure and volcano basal boundary conditions: keys to
1521 the structural evolution of large volcanic edifices on the terrestrial planets. In Platz, T.,
1522 Massironi, M., Byrne, P. K. & Hiesinger, H. (Eds.), *Volcanism and Tectonism Across the Inner*
1523 *Solar System. Geological Society, London, Special Publications* (Vol. 401, pp.219-237).
1524 <http://dx.doi.org/10.1144/SP401.7>
- 1525 McKinnon, W. B., Zahnle, K. J., Ivanov, B. A., & Melosh, H.J. (1997), Cratering on Venus—
1526 Models and observations. In S. W. Bougher, D. M. Hunten, & R. J. Phillips (Eds.), *Venus II—*
1527 *Geology, geophysics, atmosphere, and solar wind environment* (Vol. 1, pp. 969–1014). Tucson,
1528 AZ: University of Arizona Press.
- 1529 Moore, H. J., Schenk, P. M., & Weitz, C. M. (1992), An explosive eruption on Venus, *LPSC*
1530 *Conference 23*, 927–928.
- 1531 Moore, W. B., Simon, J. I., & Webb, A. A. G. (2017). Heat-pipe planet. *Earth and Planetary*
1532 *Science Letters*, 474, 13–19. <https://doi.org/10.1016/j.epsl.2017.06.015>
- 1533 Nimmo, F., & McKenzie, D. (1998). Volcanism and tectonics on Venus. *Annual Review of Earth*
1534 *and Planetary Sciences*, 26(1), 23–51. <https://doi.org/10.1146/annurev.earth.26.1.23>
- 1535 Okubo, C. H., & Martel, S. J. (1998). Pit crater formation on Kilauea volcano, Hawaii. *Journal*
1536 *of Volcanology and Geothermal Research*, 86(1-4), 1-18
- 1537 O’Rourke, J. G., & Korenaga, J. (2015). Thermal evolution of Venus with argon degassing.
1538 *Icarus*, 260, 128–140. <https://doi.org/10.1016/j.icarus.2015.07.009>
- 1539 O’Rourke, J. G., Wolf, A. S., & Ehlmann, B. L. (2014). Venus: Interpreting the spatial
1540 distribution of volcanically modified craters. *Geophysical Research Letters*, 41, 8252–8260.
1541 <https://doi.org/10.1002/2014GL062121>
- 1542 Parfitt, E. A., & Head, J.W. (1993), Buffered and unbuffered dike emplacement on Earth and
1543 Venus: Implications for magma reservoir size, depth, and rate of magma replenishment. *Earth,*
1544 *Moon, and Planets*, 61(3), 249–281.
- 1545 Peacock, D. C. P., & Sanderson, D. J (2018). Structural analyses and fracture network

- 1546 characterisation: Seven pillars of wisdom. *Earth-Science Reviews*, 184, p.13–28.
- 1547 Pettengill, G. H., Ford, P. G., & Simpson, R. A. (1996), Electrical properties of the Venus
1548 surface from bistatic radar observations, *Science*, 272, 1,628–1,631.
- 1549 Plaut, J. J. (1993) Stereo imaging, in Guide to Magellan Image Interpretation. In J. P. Ford, et al.
1550 (Eds.), *Guide to Magellan image interpretation (National Aeronautics and Space Administration*
1551 *Jet Propulsion The Laboratory Publication 93–24, 93–24)*. Pasadena, CA, NASA JPL.
- 1552 Phillips, R. J. (1990), Convection-driven tectonics on Venus. *Journal of Geophysical Research*,
1553 95(B2), 1301–1316.
- 1554 Phillips, R. J., & Hansen, V. L. (1994). Tectonic and magmatic evolution of Venus. *Annual*
1555 *Review of Earth and Planetary Sciences*, 22(1), 597–656.
1556 <https://doi.org/10.1146/annurev.earth.22.050194.003121>
- 1557 Phillips, R. J., & Hansen, V. L. (1998). Geological evolution of Venus: Rises, plains, plumes,
1558 and plateaus. *Science*, 279(5356), 1492–1497. <https://doi.org/10.1126/science.279.5356.1492>
- 1559 Phillips, R. J., & Izenberg, N. R. (1995). Ejecta correlations with spatial crater density and Venus
1560 resurfacing history. *Geophysical Research Letters*, 22(12), 1517–1520.
- 1561 Phillips, R. J., Raubertas, R. F., Arvidson, R. E., Sarkar, I. C., Herrick, R. R., Izenberg, N., &
1562 Grimm, R. E. (1992). Impact craters and Venus resurfacing history. *Journal of Geophysical*
1563 *Research*, 97(E10), 15,923–15,948. <https://doi.org/10.1029/92JE01696>
- 1564 Powell, D. (1992). Interpretation of geological structure through maps: An introductory practical
1565 manual, Longman Scientific & Technical, 176pp.
- 1566 Price, M., & Suppe, J. (1994), Mean age of rifting and volcanism on Venus deduced from impact
1567 crater densities. *Nature*, 372, 756–759.
- 1568 Price, M., & Suppe, J. (1995). Constraints on the resurfacing history of Venus from the
1569 hypsometry and distribution of volcanism, tectonism, and impact craters. *Earth, Moon, and*
1570 *Planets*, 71(1–2), 99–145. <https://doi.org/10.1007/BF00612873>
- 1571 Reese, C. C., Solomatov, V. S., & Orth, C.P. (2007), Mechanisms for cessation of magmatic
1572 resurfacing on Venus. *Journal of Geophysical Research*, 112(E04S04),
1573 doi:10.1029/2006JE002782.
- 1574 Romeo, I. (2013). Monte Carlo models of the interaction between impact cratering and volcanic
1575 resurfacing on Venus: The effect of the Beta-Atla-Themis anomaly. *Planetary and Space*
1576 *Science*, 87, 157–172. <https://doi.org/10.1016/j.pss.2013.07.010>
- 1577 Romeo, I., & Turcotte, D. L. (2010). Resurfacing on Venus. *Planetary and Space Science*,
1578 58(10), 1374–1380. <https://doi.org/10.1016/j.pss.2010.05.022>
- 1579 Romeo, I., Capote, R., & Anguita, F. (2005). Tectonic and kinematic study of a strike-slip zone
1580 along the southern margin of Central Ovda Regio, Venus—Geodynamical implications for
1581 crustal plateaux formation and evolution. *Icarus*, 175, 320–334.
- 1582 Rosenblatt, P., Pinet, P. C., & Thouvenot, E. (1994). Comparative hypsometric analysis of Earth
1583 and Venus. *Geophysical Research Letters*, 21(6), 465–468. <https://doi.org/10.1029/94GL00419>
- 1584 Ruiz, J. (2007). The heat flow during the formation of ribbon terrains on Venus. *Planetary and*
1585 *Space Science*, 55(14), 2063–2070. <https://doi.org/10.1016/j.pss.2007.05.003>

1586 Schaber, G. G., Strom, R. G., Moore, H. J., & 7 others (1992). Geology and distribution of
1587 impact craters on Venus—What are they telling us?. *Journal of Geophysical Research*, 97,
1588 13,257–13,302.

1589 Schaefer, L., & Fegley, B. (2004). Heavy metal frost on Venus. *Icarus*, 168, 215–219.

1590 Schultz, P. H. (1992). Atmospheric effects on ejecta emplacement and crater formation on
1591 Venus. *Journal of Geophysical Research*, 97, 16,183–16,248

1592 Schultz, R. A., Okubo, C. H., Goudy, C. L., & Wilkins, S. J. (2004). Igneous dikes on Mars
1593 revealed by Mars Orbiter Laser Altimeter topography. *Geology*, 32(10), 889–892.
1594 <https://doi.org/10.1130/G20548.1>

1595 Smrekar, S. E., & Phillips, R. J. (1991). Venusian highlands: Geoid to topography ratios and
1596 their implications. *Earth and Planetary Science Letters*, 107(3–4), 582–597.
1597 [https://doi.org/10.1016/0012-821X\(91\)90103-O](https://doi.org/10.1016/0012-821X(91)90103-O)

1598 Smrekar, S. E., & Stofan, E. R. (1997). Coupled upwelling and delamination: A new mechanism
1599 for corona formation and heat loss on Venus. *Science*, 277(5330), 1289–1294.
1600 <https://doi.org/10.1126/science.277.5330.1289>

1601 Smrekar, S.E., & Stofan, E. R. (1999), Origin of corona-dominated topographic rises on Venus.
1602 *Icarus*, 139, 100–116.

1603 Smrekar, S. E., Kiefer, W. S., & Stofan, E. R. (1997). Large volcanic rises on Venus. In I. S. W.
1604 Bougher, D. M. Hunten, & R. J. Phillips (Eds.), *Venus II—Geology, geophysics, atmosphere, and*
1605 *solar wind environment* (Vol. 1, pp. 845–879). Tucson, AZ: University of Arizona Press.

1606 Solomatov, V. S., & Moresi, L.-N. (1996). Stagnant lid convection on Venus. *Journal of*
1607 *Geophysical Research*, 101, 4737–4753, doi:10.1029/95JE03361.

1608 Solomon, S. C. (1993). The geophysics of Venus. *Physics Today*, 46(7), 48–55.
1609 <https://doi.org/10.1063/1.881359>

1610 Solomon, S. C., Smrekar, S. E., Bindschadler, D. L., Grimm, R. E., Kaula, W. M., McGill, G. E.,
1611 et al. (1992). Venus tectonics: An overview of Magellan observations. *Journal of Geophysical*
1612 *Research*, 97(E8), 13,199–13,255. <https://doi.org/10.1029/92JE01418>

1613 Stofan, E. R., Brian, A. W., & Guest, J. E. (2005). Resurfacing styles and rates on Venus:
1614 Assessment of 18 Venusian quadrangles. *Icarus*, 173(2), 312–321.
1615 <https://doi.org/10.1016/j.icarus.2004.08.004>

1616 Stofan, E. R., and Guest, J. E. (2003), Geologic map of the Aino Planitia quadrangle (V–46),
1617 Venus: U.S. Geological Survey Geologic Investigations Series, I–2779, scale 1:5,000,000,
1618 <https://pubs.usgs.gov/imap/i2779/>

1619 Stofan, E. R., Senske, D. A., & Michaels, G. (1993). Tectonic features in Magellan data. In J. P.
1620 Ford, et al. (Eds.), *Guide to Magellan image interpretation (National Aeronautics and Space*
1621 *Administration Jet Propulsion The Laboratory Publication 93–24*, 93–108). Pasadena, CA,
1622 NASA JPL.

1623 Strom, R. G., Schaber, G. G., & Dawson, D. D. (1994). The global resurfacing of Venus. *Journal*
1624 *of Geophysical Research*, 99(E5), 10,899–10,926. <https://doi.org/10.1029/94JE00388>

- 1625 Tanaka, K.L., Skinner, J.A. and Hare, T.M., 2009. Planetary geologic mapping handbook-2009.
1626 U.S. Geological Survey
- 1627 Tanaka, K. L., (Compiler) (1994). The Venus geologic mappers' handbook (2nd ed.): U.S.
1628 Geological Survey Open-File Report 94-438, 68 p.
- 1629 Tovar, D., Hansen, V. L., & Swenson, J. B. (2015). Preliminary detailed structural map of an
1630 equatorial fracture zone (15S–20S/110E–124E), Western Aphrodite Terra, Venus. *LPSC 46*,
1631 2555.pdf.
- 1632 Tuckwell, G. W., & Ghail, R. C. (2003). A 400-km-scale strike-slip zone near the boundary of
1633 Thetis Regio, Venus. *Earth and Planetary Science Letters*, 211(1–2), 45–55.
- 1634 Turcotte, D. L (1993). An episodic hypothesis for Venusian tectonics. *Journal of Geophysical*
1635 *Research*, 98(E9), 17061–17068.
- 1636 Turcotte, D. L., Morein, G., Roberts, D., & Malamud, B. D. (1999). Catastrophic resurfacing and
1637 episodic subduction on Venus. *Icarus*, 139(1), 49–54. <https://doi.org/10.1006/icar.1999.6084>
- 1638 U.S. Geological Survey (1998) Radar-image and shaded relief maps of the Aphrodite Planitia
1639 Region of Venus, 1:10,000,000. Map I- 2476.
- 1640 Watters, T. R. (1988). Wrinkle ridge assemblages on the terrestrial planets. *Journal of*
1641 *Geophysical Research*, 93(10), 236–254.
- 1642 Whitten J. L., & Campbell, B. A (2016). Recent volcanic resurfacing of Venusian craters.
1643 *Geology*, doi:10.1130/G37681.1.
- 1644 Wietz, C. M. (1993). Impact craters. In J. P. Ford, et al. (Eds.), *Guide to Magellan image*
1645 *interpretation (National Aeronautics and Space Administration Jet Propulsion The Laboratory*
1646 *Publication 93–24, 75-92)*. Pasadena, CA, NASA JPL.
- 1647 Wilhelms, D. E. (1972). Geologic mapping of the second planet, U.S. Geological Survey
1648 Interagency Report, Astrogeology, 55 pp.
- 1649 Wilhelms, D. E. (1990). Geologic mapping, in planetary mapping, Edited by R. Greeley and R.
1650 M. Batson, p. 296, Cambridge Univ. Pres, London.
- 1651 Williams-Jones, G., Williams-Jones, A. E., & Stix, J. (1998). The nature and origin of venusian
1652 canali. *Journal of Geophysical Research*, 3, 8,545–8,555.
- 1653 Wroblewski, F. B., Treiman, A. H., Bhiravarasu, S., & Gregg, T. K. (2019). Ovda Fluctus, the
1654 festoon lava flow on Ovda Regio, Venus: Not silica-rich. *Journal of Geophysical Research-*
1655 *Planets* 124, <https://doi.org/10.1029/2019JE006039>
- 1656 Zimbelman, J. R. (2001). Image resolution and evaluation of genetic hypotheses for planetary
1657 landscapes. *Geomorphology*, 37(3-4), 179–199. [https://doi.org/10.1016/S0169-555X\(00\)00082-9](https://doi.org/10.1016/S0169-555X(00)00082-9)

Table 1. Aphrodite Map Area Impact Craters

Name	Latitude (deg N)	Longitude (deg E)	Diameter (km)	Elevation (km)	V-map	Unit Location	Ejecta blanket	Impact halo	Central peak	Rim	Interior flooding	Crater density*	Crater data base	Deformed?	Temporal implications and comments
Abigail	-52.2	111.2	18.4	6050.84	57	Afu	Y	N	Y	Y	Y	1.59	H, S	cut by ARF & ACRW	predates ARF & ACRW
Abika	-52.5	104.4	14.5	6051.01	57	Afu	Y	N	N	Y	Y	2.23	H, S	can't tell timing with ACRW	
Addams	-56.2	98.9	87	6051.47	57	Afu	Y	N	Y	Y	Y	2.86	H, S	outflow cut by ACRW	predates ACWR
Afiba	-47.1	102.7	9.5	6051.71†	47	rti	Y	N	N	Y	N	1.59†	S	no deformation	
Agrippina	-33.2	65.7	38.6	6051.06	46	fme, fu	Y	N	Y	Y	Y	2.55	H, S	cut by ACRW?	predates ACWR
Ailar	-15.8	68.4	8.2	6051.47	34	fu	Y	N	N	Y	N	1.27	H, S	no deformation	
Alison	-4	165.6	14.4	6051.51	37	blu	Y	Y	Y	Y	Y	2.55	H, S	no deformation	
Amanda	-29.2	94.5	12.5	6052.07	47	fu	Y	N	N	Y	N	1.91†	H, S	no deformation	
Andreianova	-3	68.8	66.1	6052.97	34	rto	Y	N	Y	Y	Y	1.91	H, S	no deformation	predates Athensik
Austen	-25	168.4	45.1	6052.47	37/49	fata	Y	Y	Y	Y	N	2.86	H, S	cut by Athensik Corona structures	predates Athensik Corona
Ayana	-29.2	175.5	13.8	6051.92	49	Afu	Y	N	N	Y	Y	2.55	H, S	can't tell time wrt ACRW	composite crater formed during FZ evolution
Badarzewska	-22.6	137.2	29.6	6053.46	36	fchu	Y	N	Y	Y	Y	1.91	H, S	cuts & cut by FSZ	
Bassi	-19	64.6	31	6051.02	34	blu, fu	Y	Y	Y	Y	N	1.91	H, S	buries ACRW	postdates ACWR
Behn	-32.4	142	25.4	6052.87	48	fAa	Y	N	Y	Y	Y	1.91	H, S	ejecta cut by Artemis Chasrna faults; interior buries Artemis Chasrna	predates Artemis Chasrna; interior flooding postdates Chasrna structures
Blanche	-9.3	157	12.3	6054.08†	37	rIN	Y	N	N	Y	N	1.91†	S	tsid	
Bonnevie	-36.1	127	92.2	6052.42	48	fAa/fAa	Y	Y	Y	Y	Y	0.95	H, S	no deformation	postdates Artemis interior
Bonin	-6.3	117.6	28.5	6054.89	35	rT	Y	N	N	Y	Y	1.27	H, S	no deformation	
Boulanger	-26.6	99.2	71.5	6052.76	47	rIH	Y	N	Y	Y	N	1.91	H, S	no deformation	
Chiyojo	-47.8	95.7	40.2	6051.25	47	st	Y	N	Y	Y	Y	2.86	H, S	covers & cut by ARF; cut by ACRW	date crater; crater predates ACWR
Chloe	-7.4	98.6	18.6	6055.93	35	rTO	Y	N	Y	Y	Y	2.23	H, S	no deformation	

Corpman	0.3	151.8	46	6052.21	25/37	fSa	Y	Y	N	Y	Y	3.5	H, S	mostly in Niobe	(outflow cut by N- fractures)
Dado	-13.9	87.6	11.2	6053.06	34	fLS	Y	N	N	Y	N	1.27	H, S	no deformation	
de Beausoleil	-5	102.8	28.2	6054.93	35	rTO	Y	N	N	Y	N	2.55	H, S	no deformation	
Deloria	-32	97.1	31.9	6052.13	47	fu	Y	N	Y	Y	Y	1.91	H, S	buries fractures	postdates fractures
Dheepa	-21.6	176.3	4.7	6052.55	37	f	Y	Y	N	Y	N	1.91	H	tstd	
Eini	-41.6	96.4	5.9	6050.91	47	Afu	Y	Y	N	Y	N	2.86	H, S	tstd	
Elena	-18.3	73.4	17.6	6051.53	34	fu	Y	N	N	Y	N	1.27	H, S	fractures	buries N-trending
Elma	-10.1	91.1	10.2	6054.62	35	fLS	Y	N	N	Y	N	1.91	H, S	tstd	
Emilia	-26.5	88.2	12.5	6051.55	46	fu	Y	N	N	Y	Y	0.64	H, S	& ARF	buries ENE-fractures
Fava	-0.7	87.4	9.7	6055.28	34	rTO	Y	N	N	Y	Y?	2.23	H, S	tstd	postdates ARF
Florence	-15.2	85	10.5	6052.89	34	fu	Y	N	N	Y	N	1.27	H, S	no deformation	
Fredegonde	-50.5	93.3	25.2	6051.55	57	Afu	Y	Y	Y	Y	Y	2.55	H, S	buries ACRW?	postdates ACWR?
Fukiko	-23.1	105.8	13.9	6052.6	35	fg	Y	N	N	Y	Y	2.55	H, S	FZS/CCS	outflows bury
Germain	-37.9	63.7	35.5	6051.09	46	st	Y	Y	Y	Y	Y	2.55	H, S	lineaments?	possibly deformed
Gilmore	-6.7	132.8	21.3	6055.25	36	rTT	Y	N	N	Y	Y	1.59	H, S	cut by ARF	post TT, pre-ARF or late ARF
Gulnara	-23.7	174	5	6051.68	37	fAta	Y	N	N	Y	N	1.91†	S	tstd	
Hadisha	-39	97.2	8.9	6051.25	47	st	Y	Y	N	Y	Y	2.55	H, S	troughs	fills existing fracture
Halle	-19.8	145.5	21.5	6052.99	36	f	Y	Y	N	Y	Y	1.59	H, S	FZS/CCS	covers & cut by
Hanka	-27.3	114.3	5	6053.29	47	fchu	Y	N	N	Y	N	1.59	H, S	no deformation	formed during FZ/CC evolution
Helga	-10.4	116.7	8.8	6054.28	35	rTT	Y	N	N	Y	N	0.95	H, S	no deformation	postdates FZ
Hennie	-51.9	146	70.4	6050.96	58	st	Y	N	Y	Y	Y	1.91	H, S	buries ARF	postdates ARF
Howe	-45.7	174.8	38.6	6051.42	49	st	Y	N	Y	Y	Y	1.59	H, S	ejecta cut by ACWR?	predates ACWR?
Huang Daopo	-54.2	165.3	29.1	6051.94	58	st	Y	N	N	Y	Y	2.86	H, S	cut by ARF	predates ARF
Imagmi	-48.4	100.7	7.6	6050.82	47	Afu	Y	Y	N	Y	N	2.55	H, S	flows into ARF	postdates ARF
Irma	-50.9	122	9.5	6051.23	58	Afu	Y	Y	N	Y	N	2.55	H, S	no deformation	composite crater
Istady	-51.8	132.6	5.4	6051.18	58	Afu	Y	Y	N	Y	N	2.23	H, S	tstd	
Izudyr	-53.9	135.2	6.6	6050.93	58	st	Y	Y	N	Y	Y	2.55	H, S	tstd	

Jalguirk	-42.3	125.1	7.5	6052.51	48	Atu	Y	N	N	Y	N	1.59	H, S	burres FZS	postdates FZ
Janina	-2	135.7	9.3	6053.27	36	fBb	Y	Y	N	Y	Y	1.91	H, S	burres FZS	postdates FZ
Janyl	-28	138.8	5.6	6053.03	48	fAb	Y	N	N	Y	N	1.59	H, S	tstd	
Jennifer	-4.6	99.8	9.6	6055.21	35	rTO	Y	N	N	Y	N	2.86	H, S	tstd	likely postdates rTO
Jhivad	-16.8	105.6	50.2	6053.48	35	f11a, blu	Y	N	Y	Y	Y	0.95	H, S	burres FZ troughs	postdates FZ
Jodi	-35.7	68.7	10.2	6051.18	46	st	Y	N	N	Y	N	2.55	H, S	burres ACRW?	postdates ACWR?
Joliot-Curie	-1.6	62.4	91.1	6052.48	34	rTO, ihtM, dD	Y	N	Y	Y	Y	1.91	H, S	not deformed?	predates dD?
Judith	-29.1	104.5	16.6	6052.71	47	st	Y	Y	N	Y	Y	2.23	H, S	burres fractures & canali	postdates fractures & canali
Jurnaisat	-15.1	135.6	7.5	6054.08	36	rTT	Y	N	N	Y	Y	0.95	H, S	tstd	
Jutta	0	142.6	7	6052.4	24/36	st	Y	N	N	Y	N	2.23	H	tstd	
Kaikiani	-32.8	163.2	19.9	6051.76	49	Atu	Y	Y	Y	Y	Y	2.23	H, S	burres ARF	postdates ARF
Kastusha	-28.6	59.9	13	6051.23	45/46	fu	Y	Y	N	Y	N	2.55	H	no deformation	
Katya	-29.5	108.7	9.2	6052.64	47	fchu	Y	Y	N	Y	N	1.59	H, S	burres FZS	postdates FZ
Khelifa	-1.5	129.9	10.8	6054.76	36	rTT	Y	N	N	Y	N	1.59	H, S	cut by ARF	predates ARF
Langtry	-17	155	50.3	6052.08	37	fchu	Y	N	N	Y	Y	1.59	H, S	cut by FZS	predates FZ
Larisa	-18.47	131.06	3.7	6054.31†	36	f†	Y	N	N	Y	N	1.59†	S	tstd	
Lazarus	-52.9	127.2	24.2	6051.25	58	st	Y	Y	Y	Y	Y	2.23	H, S	burres ARF	postdates ARF
Laila	-44.2	86.8	18.8	6051.04	46	Atu	Y	Y	Y	Y	Y	2.23	H, S	burres ACRW	postdates ACWR
Leona	-3.1	169	3	6051.57	37	fE	Y	N	N	Y	N	2.86	H	tstd	
Ma Shouzhen	-35.7	92.5	18.9	6051.8	47	Atu	Y	Y	Y	Y	Y	1.59	H, S	burres ARF & ACRW	postdates ACWR
Makola	-3.8	106.7	16.6	6053.96	35	rTO	Y	N	N	Y	N	2.23	H	does not looked deformed	
Maltby	-23.3	119.7	36.6	6053.4	35	f11b, f1c	Y	N	N	Y	Y	0.64	H	cut by FZS (stopping)	predates FZ
Mansa	-33.9	63.4	8.1	6051.08	46	fu	Y	N	N	Y	N	2.86	H	covers ACRW? tstd	indeterminate
Markham	-4.1	155.6	71.8	6051.97	37	fSa	Y	Y	Y	Y	Y	1.91	H, S	ARF & bank against ACRW	postdates ARF & ACWR
Martinez	-11.7	174.7	23.5	6052.6	37	fK	Y	N	Y	Y	N	0.64	H, S	both covers and cut by FZS	formed during FZ evolution
Maurea	-39.5	69.1	9.9	6051.52	46	fCoa	Y	Y	N	Y	Y	2.23	H, S	no deformation	
Ndella	-15.9	60.7	5.9	6051.22	34	rTM	Y	N	N	Y	N	1.91	H, S	tstd	
Ngao	-53.3	61.8	9.5	6052.64	57	fMdb	Y	Y	N	Y	Y	1.91	H, S	burres FZS	postdates FZ

O'Connor	-26	143.9	30.4	6052.43	48	fchu	Y	N	Y	Y	Y	2.55	H, S	pos. fracture reactivation?	formed late during FZ evolution?
Onissa	-25.6	150.2	8.2	6052.17	49	ff	Y	Y	N	Y	N	1.59	H, S	outflow locally buried	postdates FZ; cc
Opika	-57.1	151.9	9.8	6050.83	58	st	Y	N	N	Y	N	3.18	H	no deformation?	
Parshan	-0.2	146.5	6.8	6052.23	24/36	st	Y	N	N	Y	N	2.23	H, S	tstd	postdates fractures?
Patmat	-1.3	156.5	5.1	6051.84	37	fSa	Y	N	N	Y	N	1.91	H, S	tstd	postdates ACWR?; cc
Pavinka	-25.5	158.7	7.5	6053.22	49	blu	Y	N	N	Y	N	3.18	H, S	cut by FSZ/CC	predates FZ/CC
Philomena	-40.7	151.9	14.8	6051.63	49	Atu	Y	Y	N	Y	Y	0.95	H, S	buries ARF; buries ACWR?	postdates ACWR?
Qarlygha	-33	162.9	9.3	6051.66	49	Atu	Y	Y	N	Y	N	2.23	H, S	covers ARF	postdates ARF
Quimby	-5.7	76.7	23.2	6054.24	34	rO	Y	N	Y	Y	N	0.64	H, S	no deformation	postdates rO
Radhika	-30.3	166.4	7.9	6052.33	49	Atu	Y	N	N	Y	N	2.55	H, S	no deformation?	postdates FZ?
Raki	-49.4	70	7.5	6052.23	46	fMrdb	Y	Y	N	Y	N	1.27	H, S	buries ARF	postdates ARF
Ruit	-25.5	72.9	6.4	6051.29	46	st	Y	Y	N	Y	N	0.95	H, S	tstd	
Safarmo	-10.8	161.4	7.4	6052.3	37	fMa	Y	N	Y	Y	N	1.91	H, S	tstd	
Salka	-5	97.7	12.5	6055.53	35	rO	Y	N	N	Y	N	3.18	H, S	no deformation	
Saminlang	-39	80.7	25.9	6051.37	46	Atu	Y	N	Y	Y	Y	1.91	H, S	buries ARF	postdates ARF
Shushan	-43.8	70.2	8.5	6051.52	46	fCoa	Y	N	N	Y	N	1.91	H, S	cut by ACRW	predates ACWR
Simonenko	-26.9	97.6	31.9	6052.48	47	fu, fTh	Y	Y	Y	Y	Y	1.91	H, S	buries NE-fractures	postdates FZ
Sullivan	-1.4	110.9	32	6052.55	35	rO	Y	N	Y	Y	Y	1.27	H, S	no deformation	
Tehina	-30.4	76.4	5.4	6051.08	46	st	Y	N	N	Y	N	1.27	H, S	tstd	
Temou	-10	83.4	9.3	6055.18	34	rO	Y	N	N	Y	N	1.91†	H, S	no deformation	
Teumere	-38.3	88.1	5.4	6051.09	46	fKu	Y	N	N	Y	N	1.91	H, S	tstd	
Teura	-12.3	90.2	9.3	6054.42	35	fLS	Y	N	N	Y	N	1.27	H, S	cut by lava channel	predates lava channel
Ulpu	-35.7	179	7	6051.48	49	Atu	Y	N	N	Y	N	1.27	H, S	tstd	cc
unnamed a	-46.3	125.6	5.4	6051.79	48	st	Y	Y	N	Y	N	2.23	H, S	tstd	
unnamed b	-26.5	167.9	5.4	6052.78	49	fAla	Y	N	N	Y	N	2.86	H, S	tstd	
unnamed c	-56.9	160.5	7	6051.27	58	st	Y	N	N	Y	N	2.86	H, S	tstd	
unnamed d	-10.9	173.7	2.7	6054.538	37	fK	Y	N	N	Y	N	1.27†	S	tstd	
unnamed e	-41.9	149.6	6.4	6051.66	48	Atu	Y	Y	N	Y	N	0.96†	H, S	tstd	
unnamed f	-22.98	150.9	3.4	6052.47	37	fchu	Y	Y	N	Y	N	2.23†	H, S	tstd	

buries local fractures;

pos. fracture reactivation? formed late during FZ evolution?

outflow locally buried postdates FZ; cc

H, S FZS no deformation? postdates fractures?

H, S tstd postdates ACWR?; cc

H, S cut by FSZ/CC predates FZ/CC

buries ARF; buries ACWR? postdates ACWR?

H, S covers ARF postdates ARF

H, S no deformation postdates rO

H, S no deformation? postdates FZ?

H, S buries ARF postdates ARF

H, S tstd

H, S tstd

H, S no deformation

H, S buries ARF postdates ARF

H, S cut by ACRW predates ACWR

H, S buries NE-fractures postdates FZ

H, S no deformation

H, S tstd

H, S no deformation

H, S tstd

H, S cut by lava channel predates lava channel

H, S tstd

H, S tstd

H, S tstd

H, S tstd

S tstd

H, S tstd

H, S tstd

unnamed g	-26.1	130.4	6.3	6053.48	48	fAb	Y	Y	N	Y	N	1.59†	H ₁ S	tstd	
unnamed h	-41.5	142.9	8.2	6052.3	48	fAu	Y	Y	N	Y	N	0.95	H ₁ S	tstd	
unnamed i	-55.4	129	14.3	6051.03	58	st	Y	Y	N	Y	N	2.23	H ₁ S	tstd	composite crater
unnamed j	-39.3	110	6.3	6051.7	47	st	Y	Y	N	Y	N	0.64	H ₁ S	tstd	
unnamed k	-13.7	131.6	8.4	6054.51†	36	f1b	Y	N	N	Y	N	1.59†		tstd	
Valadon	-49	167.7	25.2	6051.71	49	st	Y	N	Y	Y	Y	1.91	H ₁ S	ARF?	covers or cut by
Veronica	-38.1	124.6	17.9	6052.4	48	fAb	Y	N	N	Y	Y	1.27	H ₁ S	undeformed (?)	formed during FZ/CC
Warren	-11.7	176.5	50.9	6052.44	37	fSi	Y	N	Y	Y	Y	0.95	H ₁ S	FZ/CC	covers & cut by
Whiting	-6.1	128	35.7	6054.73	36	rT	Y	N	Y	Y	N	1.27	H ₁ S	cut by ARF?	predates ARF?
Whitney	-30.2	151.3	42.5	6052.15	49	fCh	Y	N	Y	Y	N	1.59	H ₁ S	cut by FZS/CC	predates FZ/CC
Winnemucca	-15.4	121.1	30.3	6053.36	36	rT, fCh	Y	N	N	Y	N	1.27†	H ₁ S	cut by FZS/CC	predates FZ/CC
Xiao Hong	-43.5	101.7	38.7	6050.8	47	fAu	Y	Y	Y	Y	Y	2.55	H ₁ S	cut by ACRW?	predates ACRW?
Yasuko	-26.1	169	10.6	6053.12	49	fAla	Y	N	N	Y	N	2.86	H ₁ S	covers Atahensik fractures	postdates Atahensik Corona
Yokhtik	-50.1	158.1	11.4	6051.66	58	bst	Y	N	N	Y	Y	2.23	H ₁ S	cut by ARF	predates ARF
Yonile	-27.3	138.7	13.6	6053.03	48	fAb	Y	Y	N	Y	N	1.59	H ₁ S	no deformation	
Yonge	-14	115.1	42.8	6053.82	35	fCh	Y	N	Y	Y	N	1.27	H ₁ S	cut by FZS	predates end of FZ
Zeinab	-2.2	159.6	12.5	6051.38	37	fE	Y	N	N	Y	Y	2.86	H ₁ S	covers ACRW?	postdates ACRW?
Zemifra	-46.2	157.7	11.4	6051.28	49	st	Y	N	N	Y	Y	1.59	H ₁ S	no deformation	
Zosia	-18.9	109.2	10.5	6053.03	35	f1a	Y	N	N	Y	N	1.27	H ₁ S	determine	poor imagery; can't
Zulma	-7.7	102	11	6055.15	35	rO	Y	N	N	Y	N	1.91	H ₁ S	no deformation	

Abbreviations: N, no; Y, yes; ACRW,Artemis concentric wrinkle ridges;ARF, Artemis radial fractures; CCS, corona-chasma structures;

FZS, fracture zone structures; FZ/CC, fracture zone-corona-chasma; tstd, too small to determine; cc, composite crater

Venus crater data bases: S, Schaber et al. [1992]; H, Herrick et al. [1997]

*Crater density values from Herrick et al. [1997] at a crater's location. Value is the density of craters in the neighborhood of the specified crater;

† that is, the number of craters (including the specified crater) within a 1000 km radius circle normalized to give the number of craters per 1×10^6 km².

‡ Values calculated using the methodology of Herrick et al. [1997].